

AD-A090 048

SRI INTERNATIONAL MENLO PARK CA

F/6 4/1

THE GROWTH AND DECAY OF EQUATORIAL BACKSCATTER PLUMES. (U)

DNA001-79-C-0153

FEB 80 R T TSUNODA

UNCLASSIFIED

DNA-5249T

NL

Loc 1
40 A
C937245



END
DATE
FILED
11-80
DTIC

(12)

LEVEL II

DNA 5249T

AD A 090048

THE GROWTH AND DECAY OF EQUATORIAL BACKSCATTER PLUMES

Roland T. Tsunoda
SRI International
333 Ravenswood Avenue
Menlo Park, California 94025

1 February 1980

Topical Report for Period 1 July 1979—1 October 1979

CONTRACT No. DNA 001-79-C-0153

APPROVED FOR PUBLIC RELEASE;
DISTRIBUTION UNLIMITED.

THIS WORK SPONSORED BY THE DEFENSE NUCLEAR AGENCY
UNDER RDT&E RMSS CODE B322079462 125AAXHX64009 H2590D.

Prepared for
Director
DEFENSE NUCLEAR AGENCY
Washington, D. C. 20305

MC FILE COPY

DTIC
ELECTED
S OCT 9 1980 D
B

80 9 11 022

Destroy this report when it is no longer
needed. Do not return to sender.

PLEASE NOTIFY THE DEFENSE NUCLEAR AGENCY,
ATTN: STTI, WASHINGTON, D.C. 20305, IF
YOUR ADDRESS IS INCORRECT, IF YOU WISH TO
BE DELETED FROM THE DISTRIBUTION LIST, OR
IF THE ADDRESSEE IS NO LONGER EMPLOYED BY
YOUR ORGANIZATION.



UNCLASSIFIED

SECURITY CLASSIFICATION OF THIS PAGE (When Data Entered)

REPORT DOCUMENTATION PAGE		READ INSTRUCTIONS BEFORE COMPLETING FORM
1. REPORT NUMBER ⑮ DNA 15249T	2. GOVT ACCESSION NO. AD-A090 048	3. RECIPIENT'S CATALOG NUMBER
4. TITLE (and Subtitle) ⑯ THE GROWTH AND DECAY OF EQUATORIAL BACKSCATTER PLUMES.	5. TYPE OF REPORT & PERIOD COVERED Topical Report, period 1 July 1979 - 1 October 1979	
6. PERFORMING ORG. REPORT NUMBER SRI Project 8164	7. CONTRACT OR GRANT NUMBER(s) DNA 001-79-C-0153	
8. AUTHOR(s) ⑩ Roland T. Tsunoda	9. PERFORMING ORGANIZATION NAME AND ADDRESS SRI International 333 Ravenswood Avenue Menlo Park, California 94025	
10. CONTROLLING OFFICE NAME AND ADDRESS Director Defense Nuclear Agency Washington, D.C. 20305	11. PROGRAM ELEMENT, PROJECT, TASK AREA & WORK UNIT NUMBERS Subtask I25AAXHX64009-09	
12. REPORT DATE ⑭ 7 610	13. NUMBER OF PAGES 54	
14. MONITORING AGENCY NAME & ADDRESS (if different from Controlling Office)	15. SECURITY CLASS (of this report) UNCLASSIFIED	
	15a. DECLASSIFICATION/DOWNGRADING SCHEDULE ⑮ 55	
16. DISTRIBUTION STATEMENT (of this Report) Approved for public release; distribution unlimited.		
17. DISTRIBUTION STATEMENT (of the abstract entered in Block 20, if different from Report)		
18. SUPPLEMENTARY NOTES This work sponsored by the Defense Nuclear Agency under RDT&E RMSS Code B322079462 I25AAXHX64009 H2590D		
19. KEY WORDS (Continue on reverse side if necessary and identify by block number) Equatorial Spread F Plasma bubbles Ionospheric irregularities		
20. ABSTRACT (Continue on reverse side if necessary and identify by block number) During the past three years, the Defense Nuclear Agency (DNA) has conducted a series of rocket experiments from the Kwajalein Atoll, Marshall Islands, to investigate the character of intense, scintillation-producing irregularities that occur in the nighttime equatorial ionosphere. Because the source mechanism of equatorial irregularities, believed to be the Rayleigh-Taylor instability, is analogous to that which generates plasma-density striations in a nuclear-induced environment, there is considerable		

X 610 048 414 281

46

UNCLASSIFIED

SECURITY CLASSIFICATION OF THIS PAGE(When Data Entered)

20. ABSTRACT (Continued)

interest in the underlying physics that controls the characteristics of these irregularities. A primary objective of ALTAIR investigations of equatorial irregularities is to seek an understanding of the underlying physics by establishing the relationship between meter-scale irregularities (detected by ALTAIR), and large-scale plasma-density depletions (or "bubbles") that contain the kilometer-scale, scintillation-producing irregularities.

In this report, we describe the time evolution of backscatter "plumes" produced by one-meter equatorial field-aligned irregularities. Using ALTAIR, a fully steerable backscatter radar, to repeatedly map selected plumes, we characterize the dynamic behavior of plumes in terms of a growth and a decay phase. Most of the observed characteristics are found to be consistent with equatorial-irregularity generation predicted by current theories of Rayleigh-Taylor and gradient-drift instabilities. However, other characteristics have been found that suggest key roles played by the eastward neutral wind and by altitude-modulation of the bottomside F layer in establishing the initial conditions for plume growth. In particular, we hypothesize that a preferred vector relationship between the electric field and the plasma-density gradient (in the bottomside F layer) contributes to the apparent variability in plume growth and decay characteristics.

UNCLASSIFIED

SECURITY CLASSIFICATION OF THIS PAGE(When Data Entered)

CONTENTS

LIST OF ILLUSTRATIONS	2
I INTRODUCTION	3
II EXPERIMENTAL CONSIDERATIONS	5
III GROWTH-PHASE CHARACTERISTICS	7
A. 23 August 1977 (0830-0850 UT)	7
B. 8 August 1978 (0818-0827 UT)	12
C. 18 August 1978 (0745-0830 UT)	16
D. Summary of Growth-Phase Characteristics	20
IV DECAY-PHASE CHARACTERISTICS	22
A. 26 August 1977 (0935-1026 UT)	22
B. 8 August 1978 (1000-1100 UT)	25
C. 1 August 1978 (1207-1237 UT)	27
D. Summary of Decay-Phase Characteristics	30
V DISCUSSION AND CONCLUSIONS	31
A. Initial Conditions for Plume Development	31
B. Growth Velocity of Backscatter Plumes	38
C. Backscatter Strength of Plumes	40
D. A Working Model of Plume Growth and Decay	42
REFERENCES	44

Accession For	
NTIS GRA&I <input checked="" type="checkbox"/>	
DTIC TAB <input type="checkbox"/>	
Unannounced <input type="checkbox"/>	
Justification _____	
By _____	
Distribution/ _____	
Availability Codes _____	
Dist	Avail and/or Special
A	

ILLUSTRATIONS

1	ALTAIR East-West Scan Geometry	6
2	A Sequence of ALTAIR Maps Showing Plume Generation and Growth--23 August 1977 (0830-0850 UT)	8
3	Plume Generation from an Altitude-Modulated, Bottomside Backscatter Region--8 August 1978 (0818-0827 UT)	13
4	Example of a Plume During Initial Development--18 August 1978 (0803 UT)	17
5	Sunlit F-Layer Electron-Density Profiles--18 August 1978 (0745-0749 UT)	18
6	Electron-Density Profiles Showing a Depletion Associated with Plume Development--18 August 1978 (0803-0815 UT) . . .	20
7	A Sequence of ALTAIR Maps Showing Plume Decay--26 August 1977 (0935-1026 UT)	23
8	A Sequence of ALTAIR Maps Showing Plume Decay--8 August 1978 (1000-1100 UT)	26
9	A Sequence of ALTAIR Maps Showing Plume Decay--1 August 1978 (1207-1237 UT)	28
10	Spatial Distribution of Growth Rate and Backscatter Strength Produced by (a) an Upward-Moving F Layer, (b) a High F Layer, and (c) an Eastward Neutral wind . . .	33

I INTRODUCTION

Current theoretical understanding of the development of equatorial irregularities is that large-scale (10 to 100 km) plasma-depleted regions, or "bubbles," originate in the bottomside of the nighttime F layer via the Rayleigh-Taylor instability, and then evolve through nonlinear processes into the topside of the F layer. Theoretical models of rising plasma bubbles have been developed by several researchers (Scannapieco and Ossakow, 1976; Ossakow and Chaturvedi, 1978; Ott, 1978; Anderson and Haerendel, 1979). In the process of upward transport, steep gradients in plasma density are believed to form, leading to the generation of smaller-scale irregularities (e.g., Balsley et al., 1972; Haerendel, 1974; Hudson and Kennel, 1975).

These theoretical models appear to be generally consistent with available experimental evidence. Plasma bubbles have been measured in-situ by satellites and rockets (Hanson and Sanatani, 1974; McClure et al., 1977; Kelley et al., 1976; Morse et al., 1977). From these measurements, we have become aware of the size and percentage depletion of plasma bubbles. That plasma bubbles originate at lower altitudes was first inferred by the presence of heavy ions (Fe^+ , NO^+) within the bubbles (Hanson and Sanatani, 1973). More recently, large upward ion velocities were measured within plasma bubbles by McClure et al. (1977), which indicated that plasma bubbles did indeed move upward through the F layer. However, because of the inherent nature of satellite and rocket measurements, what is not yet known is the time evolution of these plasma bubbles and associated plasma density irregularities.

In addition to in-situ data, much of our progress in the understanding of equatorial spread-F phenomena has resulted from VHF backscatter radar measurements (e.g., Farley et al., 1970; Woodman and La Hoz, 1976). In particular, since the discovery of backscatter "plumes" that appear to extend upward from the bottomside into the topside of the F layer (Woodman

and La Hoz, 1976), researchers have shown that these backscatter plumes appear to be spatially collocated with plasma bubbles (Tsunoda and Towle, 1979; Towle, 1979; Tsunoda, 1980 a,b). Therefore, knowledge of the time evolution of backscatter plumes can probably be used to infer the time evolution of plasma bubbles.

In this report, we analyze the growth and decay of VHF backscatter plumes using data collected with ALTAIR, a fully steerable backscatter radar located in the Kwajalein Atoll, Marshall Islands. Because of the prevailing eastward drift of ionospheric plasma at the equator (Woodman, 1972), the time development of a selected backscatter feature can be monitored only with a steerable radar. In previous papers (Tsunoda et al., 1979; Tsunoda and Towle, 1979), we showed how repeated east-west scans with ALTAIR could be used to characterize the time evolution and dynamics of equatorial irregularities.

Data collected during summer campaigns in 1977 and 1978 are used in this report to characterize the life of backscatter plumes in terms of two phases, growth and decay. We note here that the two phases refer to the life cycle of an individual backscatter plume and not to the time sectors when spread-F irregularities generally develop and decay (Basu et al., 1978).

II EXPERIMENTAL CONSIDERATIONS

ALTAIR is located on Roi-Namur Island in the Kwajalein Atoll, Marshall Islands (9.4°N , 167.5°E , geographic coordinates). The corresponding magnetic dip latitude is 4.3°N , well within the statistical occurrence region ($\pm 20^{\circ}$ dip latitude) for equatorial spread F. Data used in this report were collected during the month of August in both 1977 and 1978. To obtain the data sets presented in this report, ALTAIR (a dual-frequency radar) was operated at 155.5 MHz by transmitting a $30\text{-}\mu\text{s}$ pulse-width (4.5 km range resolution) through an antenna with a 2.8° beamwidth. The basic mode of operation consisted of an east-to-west scan maintaining the radar beam perpendicular to the geomagnetic field lines at F-region altitudes. The plane of such a scan is oriented in the geomagnetic east-west direction and perpendicular to the magnetic meridian (9°E true azimuth), intersecting the meridian at an 81° elevation angle. In 1977, the scan was made in 21 discrete steps, and in 1978 at 25 discrete steps, dwelling at each beam position for 15 s. Thus, a total angular sector of 45° was scanned in 6 minutes in 1977, and a sector of 72° was scanned in 8 minutes in 1978. The radar location and the scan geometry are shown in Figure 1. Further details regarding radar characteristics and its operation can be found in Tsunoda et al. (1979) and Towle (1979).

In addition to the east-west scans used to map backscatter from equatorial field-aligned irregularities (FAI), incoherent-scatter (IS) measurements were made in selected directions. The directions were selected so that the electron density profiles obtained would correspond to the various backscatter features mapped during the east-west scans. Tsunoda et al. (1979) showed that in the absence of backscatter from equatorial FAI, backscatter obtained with the radar beam directed perpendicular to the geomagnetic field is due to IS and consequently could be used to compute electron-density profiles. When the radar beam is directed away from perpendicular intersection with the geomagnetic

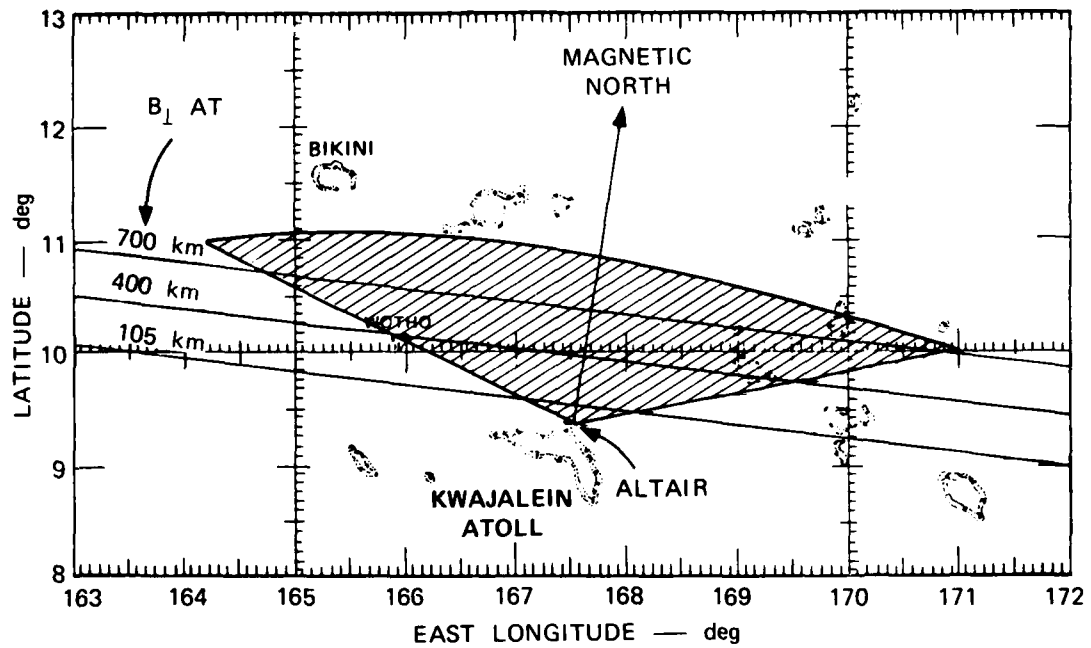


FIGURE 1 ALTAIR EAST-WEST SCAN GEOMETRY

field lines, Tsunoda (1980a,b) and Towle (1979) showed that IS measurements can be made within regions containing FAI associated with spread F. The latter type of IS measurements have been used to map plasma bubbles.

The electron density profiles used in this report were computed by averaging IS data over one-minute intervals. With a pulse repetition frequency of 40 s^{-1} , 2400 data samples were averaged, resulting in a standard deviation that is approximately 2% of the mean electron density. In the small signal-to-noise ratio (SNR) case that is applicable here, the standard deviation also varies inversely with the SNR. With a typical SNR of 0.1, the standard deviation becomes 20% of the mean electron density.

III GROWTH-PHASE CHARACTERISTICS

In this section, we present three examples that illustrate growth-phase characteristics of backscatter plumes. In all three examples, the plumes were found to be generated in the bottomside of the F layer over ALTAIR, and were found to occur very close in time to F-layer sunset. Thus, all three examples represent initial plume development for the evening. These three examples were selected from 15 nights of ALTAIR data. In the remaining data during those 15 nights, plume generation was not found to occur later in the night. That is, although plume development was observed later at night, none of the plumes were generated within the spatial sector scanned by ALTAIR. This absence of examples of plume generation later in the night is believed to have significance and is discussed in Section V.

A. 23 August 1977 (0830-0850 UT)

A time sequence of ALTAIR backscatter maps showing the initial plume development for the evening is presented in Figure 2. Each map is drawn with contours of constant backscatter strength (after range-squared correction). The 0-dB contour corresponds to backscatter that is equivalent in strength to IS from an electron density of 10^6 el/cm^3 . The other contours represent 10-dB increments in backscatter strength. Besides the above-described contours, which are used primarily to characterize backscatter plume structure, we have added the -10 dB contour (corresponding to an electron density of 10^5 el/cm^3) along the bottomside of the backscatter region to estimate the location of the bottomside of the F layer.

In the first map, taken at 0830:34 UT (universal time lags local solar time by 11 hours and 10 minutes), there is no evidence of a backscatter plume. We see only patchy backscatter occurring near the bottomside of the F layer, at around 300 km altitude. Other patchy backscatter

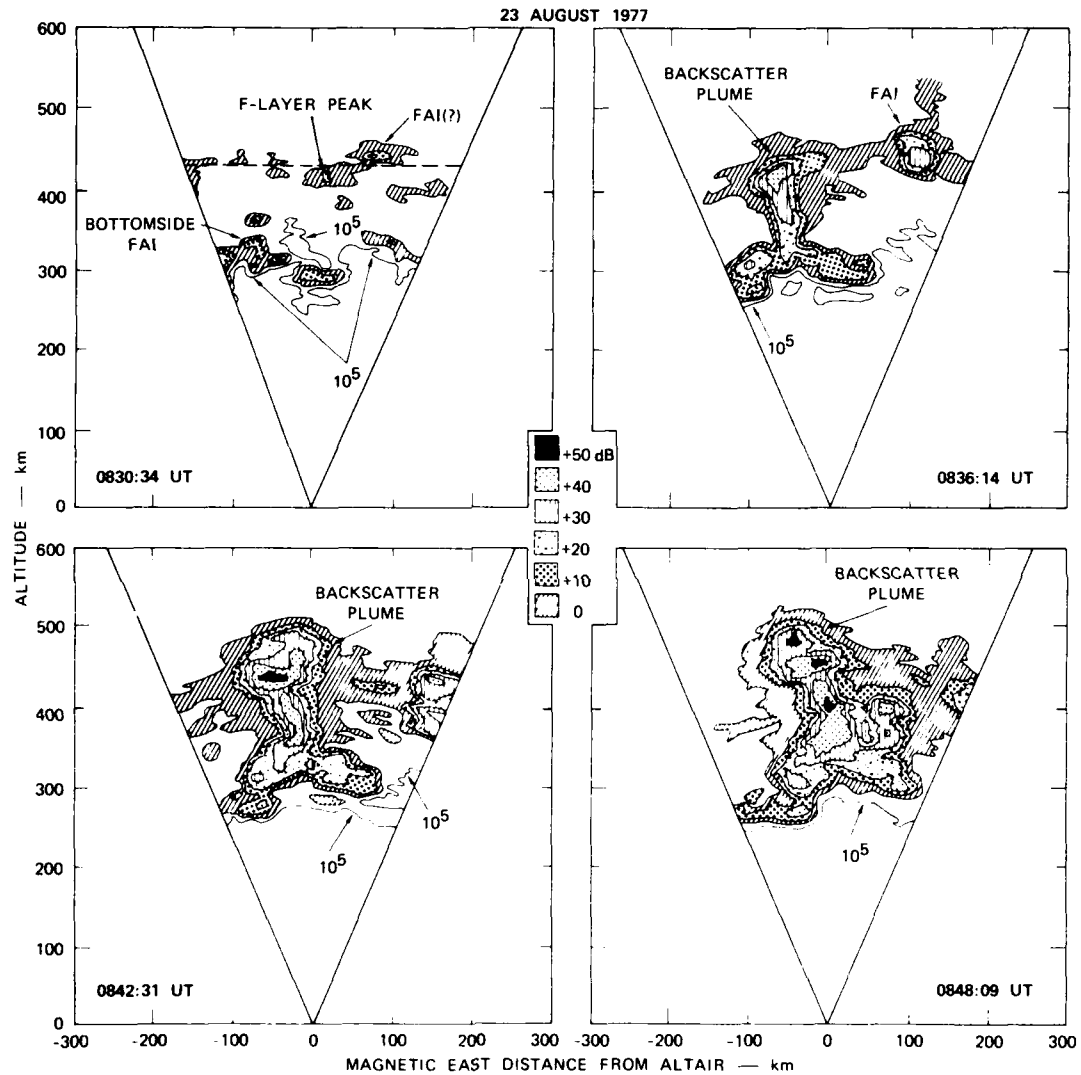


FIGURE 2 A SEQUENCE OF ALTAIR MAPS SHOWING PLUME GENERATION AND GROWTH--23 AUGUST 1977 (0830-0850 UT)

seen around 400 km altitude is mostly due to IS from the peak of the F layer where the average electron density was $\gtrsim 10^6$ el/cm³. The only evidence of high-altitude backscatter at this time is the somewhat enhanced backscatter patch labeled FAI(?) located near the F-layer peak. A similar description of ionospheric conditions was obtained from Digisonde observations made nearby (Bibl et al., 1977). The ionograms showed a quiet F layer whose bottomside rose from 250 km altitude at 0700 UT to greater than 300 km by 0800 UT. Spread F was seen to commence in ionograms taken around 0815 UT.

The first appearance of a backscatter plume is seen in the very next map, taken at 0836:14 UT, less than six minutes after the map just described. The plume is seen to extend up to the peak of the F layer (420 km) but has not yet penetrated into the topside of the F layer. It is important to point out that, prior to the appearance of the plume, a plasma depletion was not found in the vicinity of the plume shown in the second map. The absence of a plasma bubble, indicated by IS measurements, less than six minutes prior to the appearance of the plume suggests that plume backscatter must appear shortly after bubble formation and that plume growth probably maps the rise of the plasma bubble. The other examples in this section also support this line of reasoning.

The developing plume in the second map in Figure 2 is seen to be spatially connected to bottomside backscatter, a feature noted in Jicamarca radar observations that led Woodman and La Hoz (1976) to speculate that backscatter plumes (and plasma bubbles) developed upward from the bottomside of the F layer. Another feature that is characteristic of plumes is the local altitude elevation in bottomside backscatter directly beneath the point of connection. This feature is seen to persist in the remaining maps in Figure 2, and also to occur in the other examples presented in this report.

Perhaps more important is the fact that the altitude modulation of bottomside backscatter existed prior to plume development, as seen in the first map in Figure 2. Using the eastward plume displacement seen in the last three maps to estimate an eastward drift velocity, we found that the plume probably originated from the locally elevated bottomside backscatter region in the west side of the first map. The depleted (i.e.,

less than 10^5 el/cm³) region directly above the center bottomside backscatter patch is not believed to be the origin of the plume. That depleted region is believed to be part of the bottomside of the F layer, which was located around 330 km. Therefore, it appears from this example that plumes might have a tendency to grow in locations where there is a local altitude elevation in bottomside backscatter. A clear-cut case of plume development from a locally elevated, bottomside backscatter region is presented as the second example in this section. We interpret the altitude modulation in bottomside backscatter to imply a corresponding altitude modulation in the bottomside F-layer contours of constant electron density. Support for this interpretation is provided by observations of north-south-aligned 6300-A airglow depletions in the nighttime equatorial ionosphere (Weber et al., 1978). Airglow depletions have been shown to correspond to altitude modulation in electron density of the bottomside of the F layer.

Plume development, as indicated by the displacement of the top of the plume (i.e., its "head") in the sequence of maps in Figure 2, is clearly upward (and slightly westward). As a first estimate of the upward "growth velocity" of the plume, we assumed that the plume developed from the small backscatter region located at 360 km altitude in the first map, to an altitude of 420 km, which corresponds to the top of the plume head in the second map. The mean upward growth velocity is computed to be 10.6 km/min, or 176 m/s. (Selection of the small backscatter region as the probable location of plume origin is based on extrapolation using an average eastward drift velocity of 75 m/s computed from plume displacements found in the three maps in Figure 2.)

The continued upward development of the plume is seen in the third map, taken at 0842:31 UT. The plume head is seen to have grown larger and is found in the third map to have penetrated into the topside of the F layer. If we take the upward displacement of the plume head (10-dB contour) as a measure of the upward growth velocity, we obtain 9.5 km/min, or 159 m/s. This velocity is comparable to that estimated earlier using the first two maps in Figure 2.

The upward growth of the plume is seen in the third map to be associated with a continued increase in plume backscatter strength. The first appearance of the plume at 0836:14 UT was accompanied by a peak backscatter strength of 40 dB, 30 dB greater than that from bottomside backscatter seen at 0830:34 UT. As the plume developed upward, its peak backscatter strength increased by 10 dB, up to 50 dB by 0842:31 UT.

In the last map shown in Figure 2, taken at 0848:09 UT, the plume head appears to be no higher than that shown in the previous map. This sudden reduction in upward growth is seen to be accompanied by a stabilization of peak backscatter strength. It is particularly interesting to note that there is also a noticeable change in relative areas of the plume contained above and below 400 km, the nominal altitude of the F-layer peak. (The background F-layer profile was computed from IS data taken at the west edge of the last map where there was only bottomside backscatter.) We see that the neck in the bottomside F layer has continued to grow while the plume head in the topside F layer has not. The stronger irregularity-growth conditions in the bottomside F layer is attested to by the appearance of another backscatter patch next to the neck of the original plume.

After apparent completion of the generation phase, as suggested by the last map in Figure 2, the plume resumed its upward development, reaching a peak altitude of 625 km at 0927 UT. However, growth was much slower, with an average upward velocity of 2.8 km/min, or 47 m/s. This slowdown in upward growth velocity might be associated with the time that the F layer usually reverses its direction of motion from upward to downward. (This relationship is discussed in Section V.) The size of the plume head also continued to grow beyond that shown in the last map in Figure 2. The total time for the generation phase was approximately 50 minutes.

The plume development just described appears to be in accord with theoretical models of the Rayleigh-Taylor instability. The origin of a plume near a local elevation in bottomside backscatter is suggestive that a "seed" mechanism is operative that establishes the initial

conditions for plume development. The estimated upward growth velocities appear to be in accord with theoretically predicted values for bubble rise velocities, in a general sense. Whether such large velocities are expected to develop so quickly is discussed in Section V.

However, one feature contained in Figure 2 cannot be considered typical in terms of backscatter plume development. This feature is the suspected high-altitude backscatter patch [labeled FAI(?)] in the first map, which is seen in the second map to have developed into a strong backscatter region, but without any apparent connection to bottomside backscatter. Furthermore, it was not associated with any upward growth velocity. At this time, we have no good explanation for this atypical development of backscatter.

B. 8 August 1978 (0818-0827 UT)

In the first example, we described plume development that originated from a locally elevated, bottomside-backscatter region. In this second example, we present more clear-cut evidence that altitude modulation of bottomside backscatter (and probably the bottomside F-layer electron density) plays a key role in plume generation. We show that an east-west asymmetry develops in the altitude-modulated bottomside backscatter and that the asymmetry is a key feature that points to the nature of the "seed" mechanism that establishes the initial conditions for the Rayleigh-Taylor instability. We also show that the altitude modulation and asymmetry of bottomside backscatter followed by plume development results in the characteristic "fishtail" and "C-shaped" patterns found in Jicamarca radar RTI displays of 50-MHz backscatter (Woodman and La Hoz, 1976).

The backscatter maps showing plume generation on August 8 are shown in Figure 3. In the first map, taken at 0818:56 UT, we see bottomside backscatter extending across the entire east-west width of the map at around 300 km altitude. The backscatter is seen to be enhanced in the right (east) half of the map, where altitude modulation appears to be strongest. It is important to note that the enhanced backscatter region

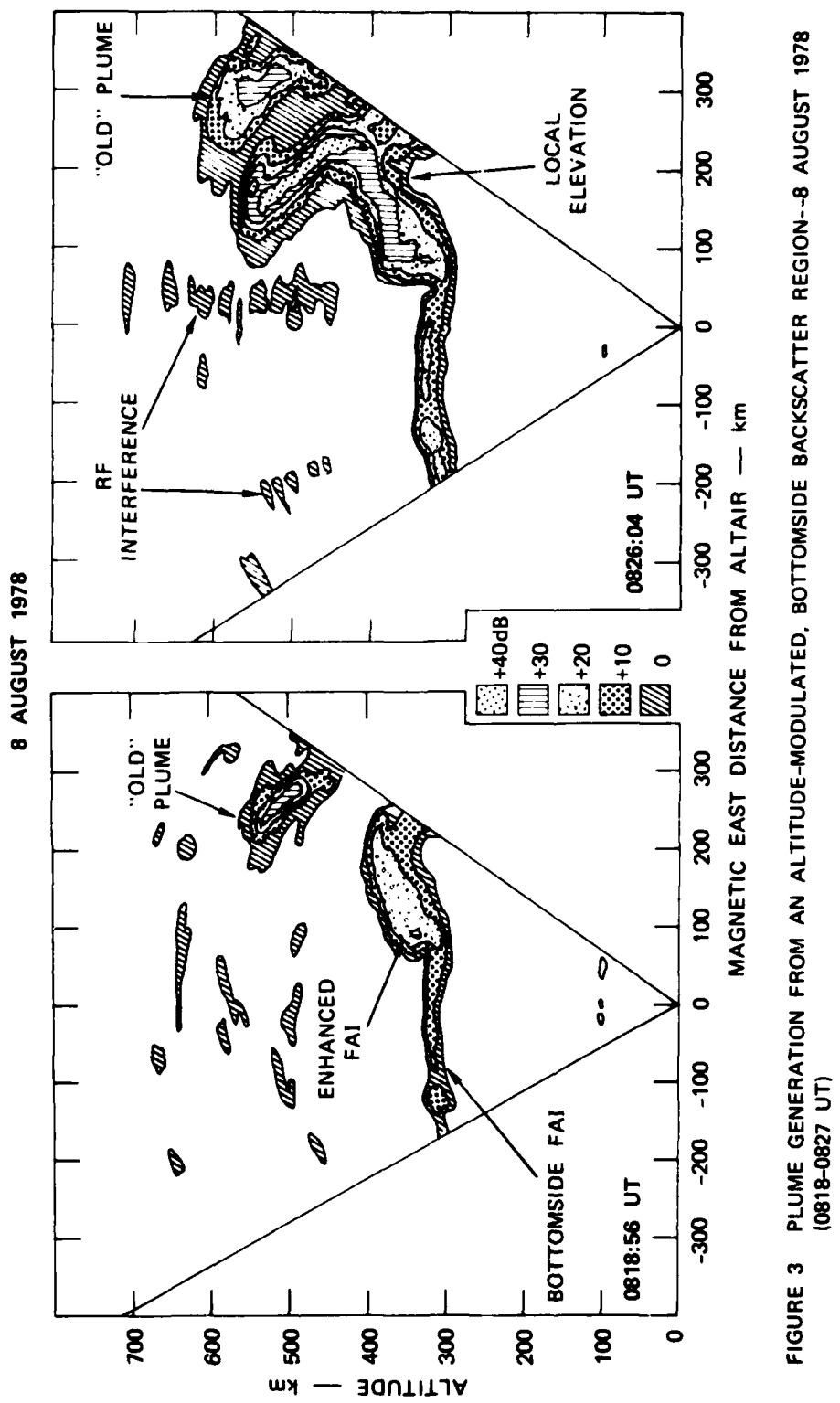


FIGURE 3 PLUME GENERATION FROM AN ALTITUDE-MODULATED, BOTTOMSIDE BACKSCATTER REGION--8 AUGUST 1978
(0818-0827 UT)

(20-dB contour) is not symmetric about the locally elevated region. Instead, the enhanced backscatter region is seen to favor the west side of the local elevation with a tilt that is east of vertical. The 20-dB contour does not extend over to the east side of the local elevation, indicating weaker irregularity-generation conditions there.

A plume is also seen at high altitudes to the east of the enhanced bottomside backscatter region. We note that the plume is tilted west of vertical while the enhanced bottomside backscatter region is tilted east of vertical. The simultaneous existence of two tilts of opposite sense indicates that the source of the tilts is altitude-dependent and is not a time-varying effect.

That the tilt is altitude-dependent is verified by the upward plume development seen in the second map in Figure 3. The second map, taken 7 minutes after the first map, shows a new plume extending upward and westward from the highest tip of the enhanced bottomside-backscatter region. The tilt of the new plume ($\sim 40^\circ$ west of vertical) is seen to be identical to that of the old plume. This repeatability of the tilt angle indicates that the conditions that determine the tilt angle have not changed. We note that the shape formed by the developing plume together with the enhanced bottomside backscatter region is the characteristic "fishtail" pattern reported by Woodman and La Hoz (1976). If bottomside backscatter was not present to the east of the plume, the pattern would resemble the "C" shape seen in Jicamarca RTIs.

Another clue as to the physics of plume generation is given by the spatial distribution of backscatter strength. Backscatter is seen to have increased by 10 dB, everywhere except in the old plume. This observation suggests that old plumes do not participate in the generation process that produces new plumes. The enhancement of backscatter strength found in both the bottomside and the new plume suggests that the bottomside backscatter region is the source region for new plumes.

We can also argue that the enhanced backscatter region seen in the first map in Figure 3 is not the developing head of the plume, but rather an enhanced part of the bottomside backscatter. This point is

important in considering the relationship of a plume to associated plasma depletions, or bubbles. To make this point, we note that backscatter is stronger in the portion of the plume tilted west of vertical than in the portion tilted east of vertical. Not only does the backscatter between those two portions differ by 10 dB, but the new plume can be considered to have increased in strength by 40 dB, whereas the bottomside-backscatter region increased in strength by only 10 dB. We interpret this to mean that the plume head and "neck" are defined by the 40-dB contour and that the eastward tilt is part of the bottomside backscatter region seen in the first map. This interpretation does not require a shear in plasma flow to account for opposite sense of the tilts.

The relationship between plumes and plasma bubbles is implicitly reflected in the independent upward growth of new and old plumes. We saw in Figure 3, rapid upward growth of a new plume in the presence of an older plume that continued to grow upward but at a much slower rate. As a conservative estimate of the upward growth velocity of the developing plume, we use the altitude extent of the 40-dB contour within the plume. Dividing the altitude extent by the time between scans, we obtain a growth velocity of 21 km/min, or 350 m/s. (This velocity is approximately twice that found in the first example.) Examination of maps taken at still later times revealed that the new plume extended to much higher altitudes than the older plume.

Because two adjacent plumes have greatly different upward growth-velocities, the apparent upward velocity is clearly not a result of simple upward transport by a large-scale electric field of 1-m FAI imbedded in a smooth and longitudinally uniform background electron density. Instead, it is probable that plumes represent tracers for upward-moving plasma bubbles that have varying percentage amounts of plasma depletions, and thus, varying rise rates because of corresponding polarization electric fields that develop within plasma bubbles. This hypothesis is consistent with the association of developing plumes with plasma bubbles shown in the third example in this section, and with the more general association of plumes and plasma bubbles shown in previous papers (Tsunoda and Towle, 1979; Towle, 1979; Tsunoda, 1980a,b).

Finally, it is important to note that the location of the local elevation kink in the height of the bottomside backscatter in the two maps in Figure 3 has not moved in east-west direction. This feature by itself does not seem especially significant. But we note that the "old" plume, in the same two maps, has drifted eastward with a velocity of 140 m/s. The point is, bottomside backscatter is not drifting eastward at the same speed as the plume. (This difference in velocity has been noted in other ALTAIR data.) This difference in irregularity-pattern drift suggests that there is either an altitude dependence of the electric field, or that a different source mechanism for bottomside and plume backscatter might be operative. We discuss the implications of these observations in Section V.

C. 18 August 1978 (0745-0830 UT)

In the first two examples, we described principal plume characteristics that are found during the generation phase. Strictly speaking, plume development simply reflects the generation of small-scale FAI and their spatial distribution as a function of time. Earlier results (Tsunoda and Towle, 1979; Towle, 1979; Tsunoda, 1980a,b) showed that plumes are spatially collocated with plasma bubbles. However, it was not demonstrated whether plumes and bubbles coexist through all phases of development and decay. In this example, we show that plumes are collocated with plasma bubbles even during the plume generation phase.

The third example of a developing backscatter plume is shown in Figure 4. The plume is seen to be similar to those shown in Figures 2 and 3 in the following ways. The plume is seen to be spatially connected to a bottomside backscatter region that is located on the west side of the locally elevated region. That is, the plume connection to its bottomside backscatter is asymmetric in the east-west direction. The connection is to the west side despite the presence of strong bottomside backscatter to the east of the local elevation. The bottomside backscatter occurs between 300 and 350 km altitude to the west of the plume, similar in altitude to that shown in Figure 3. The higher altitude of bottomside

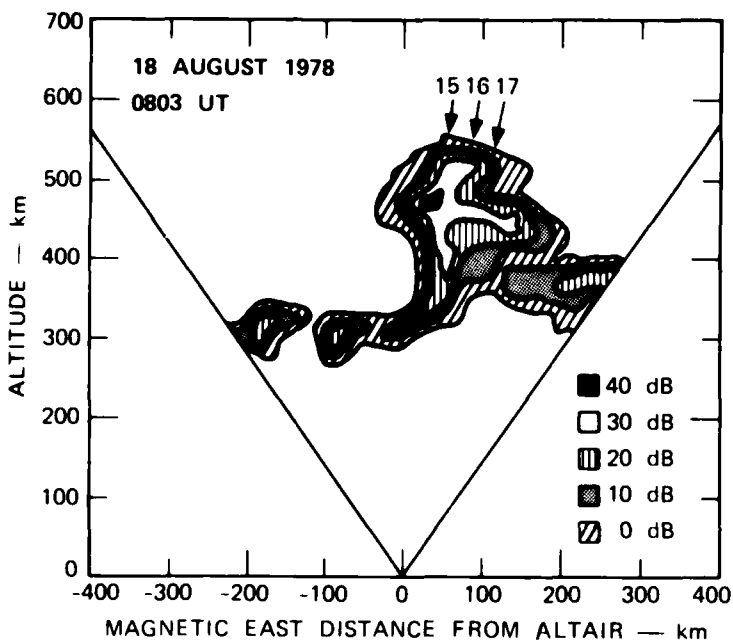


FIGURE 4 EXAMPLE OF A PLUME DURING INITIAL DEVELOPMENT--
18 AUGUST 1978 (0803 UT)

backscatter to the east of the plume is shown in following paragraphs to be a result of an upward-moving F layer. And the peak backscatter strength is 40 dB above IS level. (Later, we show that the plume in Figure 4 is also contained within the bottomside F layer.)

To illustrate that spread-F backscatter was not observed prior to 0803 UT, we present three electron-density profiles in Figure 5, obtained 14 to 18 minutes before the map shown in Figure 4. These profiles were obtained during a south-to-north latitude scan in the magnetic meridian (9° true azimuth). Each profile was computed by averaging IS data collected for one minute at each of the antenna positions shown in Figure 5. In order to use one abscissa for all three profiles, each profile taken later in time has been displaced to the right of the earlier one by one decade in electron density. The logarithmic scale as shown corresponds to the first profile taken at 0745 UT. For convenience of comparison, we have shaded the portions of the profiles that are above 10^5 el/cm^3 .

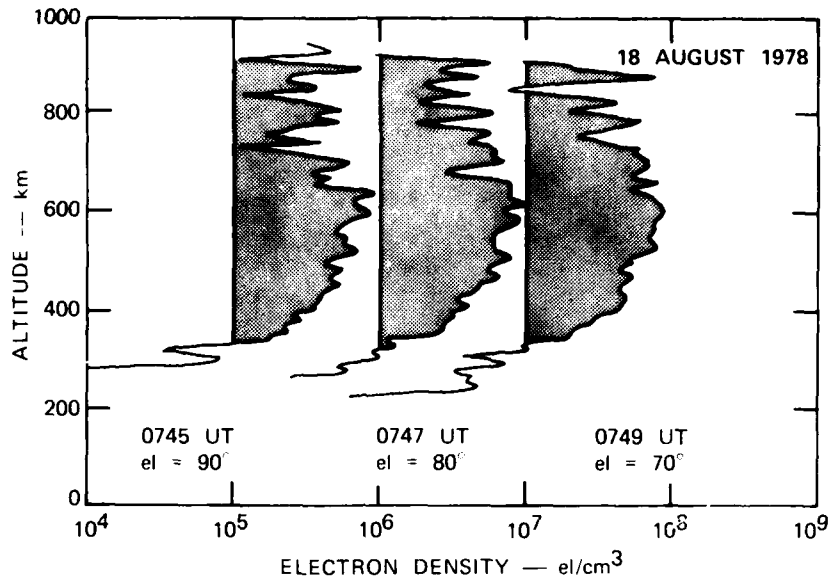


FIGURE 5 SUNLIT F-LAYER ELECTRON-DENSITY PROFILES--18 AUGUST 1978
(0745-0749 UT)

All three profiles were obtained while the solar zenith angle varied from 100° to 101.3° , with the shadow height between 100 and 150 km. All profiles display a bottomside F layer located at 300 km and a broad F-layer peak around 600 km. From these profiles, it seems clear that solar illumination at these (or larger) zenith angles does not result in any measurable (with ALTAIR) electron densities below 300 km altitude. However, the gradual slope of the bottomside profiles is consistent with a sunlit F layer at those altitudes. (The structure in the topside profiles is probably the result of poor SNRs and should not be interpreted as real structure.)

The center electron density profile in Figure 5 is of particular interest because it was obtained with the radar beam directed perpendicular to the geomagnetic field. The presence of any backscatter from FAI in this direction should have appeared in this profile. Clearly, there was no backscatter from FAI at this time. Therefore, we conclude

that the plume seen in Figure 4 did not exist at 0747 UT and that it must have developed within the following 20 minutes.

After the scan beginning at 0803 UT (Figure 4) was completed, IS measurements were made at selected off-perpendicular antenna directions corresponding to beam positions 15, 16, and 17, as shown in Figure 4. Electron-density profiles obtained from those IS measurements are shown in Figure 6 together with a fourth profile taken several minutes later. The fourth profile, taken at 0821 UT with the antenna pointed 10° south of vertical in the magnetic meridian, corresponds to a region just to the west of the plume in Figure 4 (allowing for an eastward plume drift). Comparing this fourth profile in Figure 6 to those in Figure 5, we see that they are similar except that the bottomside of the F layer has risen to 420 km altitude. We therefore use this profile as the reference profile when examining the other profiles in Figure 6 for plasma-depleted regions.

The first two profiles in Figure 6 (corresponding to beam positions 15 and 16) are seen to be highly structured, with substantial depletions at altitudes below 550 km. The depletions become even more evident when compared to the reference profile, which has been superimposed over each of the profiles as a dashed curve. The deepest depletions appear between 460 and 520 km altitude, in the bottomside F layer. However, we see that both profiles show a recovery in the electron density near the base of the F layer, indicating that the depletion is not simply an altitude modulation of the bottom of the F layer but a true developing plasma bubble. The third profile taken at 0815 UT (beam position 17) also contains structure at altitudes below 600 km but is not as plasma-depleted as the first two profiles.

The substantial plasma depletions below 550 km in the first two profiles and the less depleted third profile correspond very well with the altitude extent and spatial distribution of the head of the plume. We therefore conclude that plasma bubbles are spatially collocated with developing plumes in the bottomside F layer.

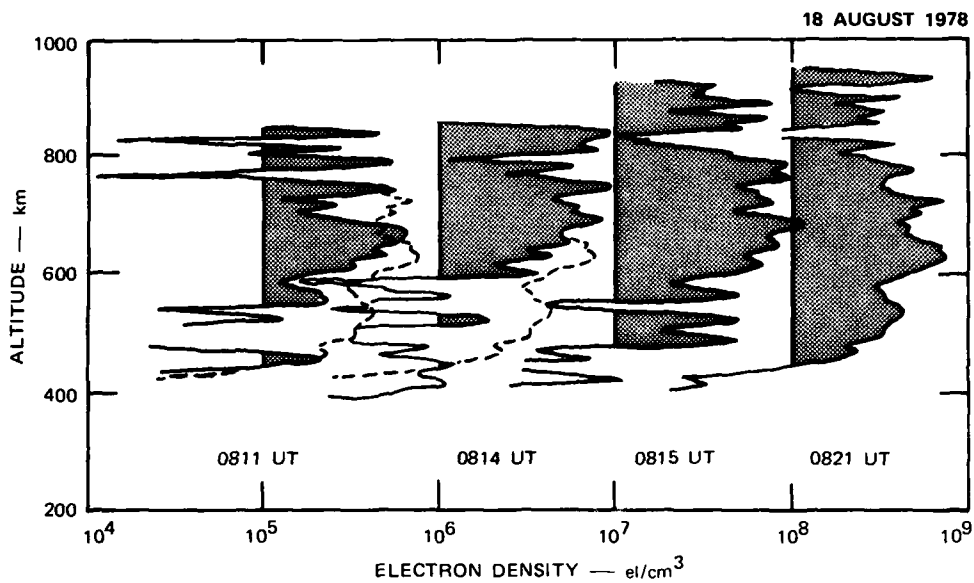


FIGURE 6 ELECTRON-DENSITY PROFILES SHOWING A DEPLETION ASSOCIATED WITH PLUME DEVELOPMENT--18 AUGUST 1978 (0803-0815 UT)

D. Summary of Growth-Phase Characteristics

From an analysis of 15 nights of ALTAIR data, including the examples presented, we have found that the following plume characteristics appear during the growth phase:

- (1) Plumes are generated primarily in the local time sector around F-layer sunset.
- (2) Plumes originate in the bottomside of the F layer.
- (3) Plumes develop where bottomside backscatter is locally elevated in altitude--by as much as 30 to 60 km.
- (4) Bottomside backscatter strength is often asymmetric in east-west direction, with stronger backscatter occurring on the west side of the local elevation.
- (5) Plumes grow upward from the bottomside into the topside of the F layer as a function of time. Upward growth velocities range from 125 to 350 m/s.
- (6) New plumes can develop in the presence of older plumes, with growth characteristics that are independent of

those of the older plumes. That is, older plumes do not appear to participate in the generation process that produces new plumes.

- (7) Backscatter strength within plumes appears to increase during upward plume development, regardless of whether the plume is in the bottomside or the topside of the F layer.
- (8) Backscatter strength stabilizes around the time when upward plume growth slows down or ceases. The plume segment contained in the bottomside F layer can continue to develop in strength and size, whereas that segment in the topside does not.
- (9) Plumes developing in the bottomside F layer are associated with plasma bubbles.
- (10) The total time for the growth phase was observed to last as long as 50 minutes.

IV DECAY-PHASE CHARACTERISTICS

As shown in the previous section, backscatter strength in plumes tends to stabilize around the time the plume approaches its maximum height. We define this time of altitude stagnation in plume growth as the end of the growth phase and the beginning of the decay phase. Although the decay phase is not as dynamic (and therefore not as likely to be studied) as the growth phase, a study of its characteristics can provide valuable insight into the source and dissipation mechanisms of plumes. We present three examples in this section to illustrate the principal characteristics.

A. 26 August 1977 (0935-1026 UT)

In this first example, we illustrate the transition from growth phase to decay phase. We show that decay does indeed begin around the time that the plume develops to maximum height. Although ALTAIR scans were not made during most of the decay phase, we were able to estimate a plume decay rate.

The backscatter maps of interest are shown in Figure 7. Only one other map was taken with ALTAIR before the first map shown in this sequence. Consequently, we do not know if other plumes had developed prior to this one. However, the backscatter patch at 600 km altitude that appears on the right edge of the first map suggests that there was prior plume activity. We do know that only one other major plume passed over ALTAIR during the remainder of the night (see Tsunoda and Towle, 1979). The plume of interest can be seen near the west edge of the first map. The bottomside of the F layer (shown by the 10^5 el/cm^3 contour) is seen in that map to be located around 400 km altitude.

In the second map, taken at 0941:18 UT, the plume is seen to be still growing as it drifts eastward toward the center of the map. The

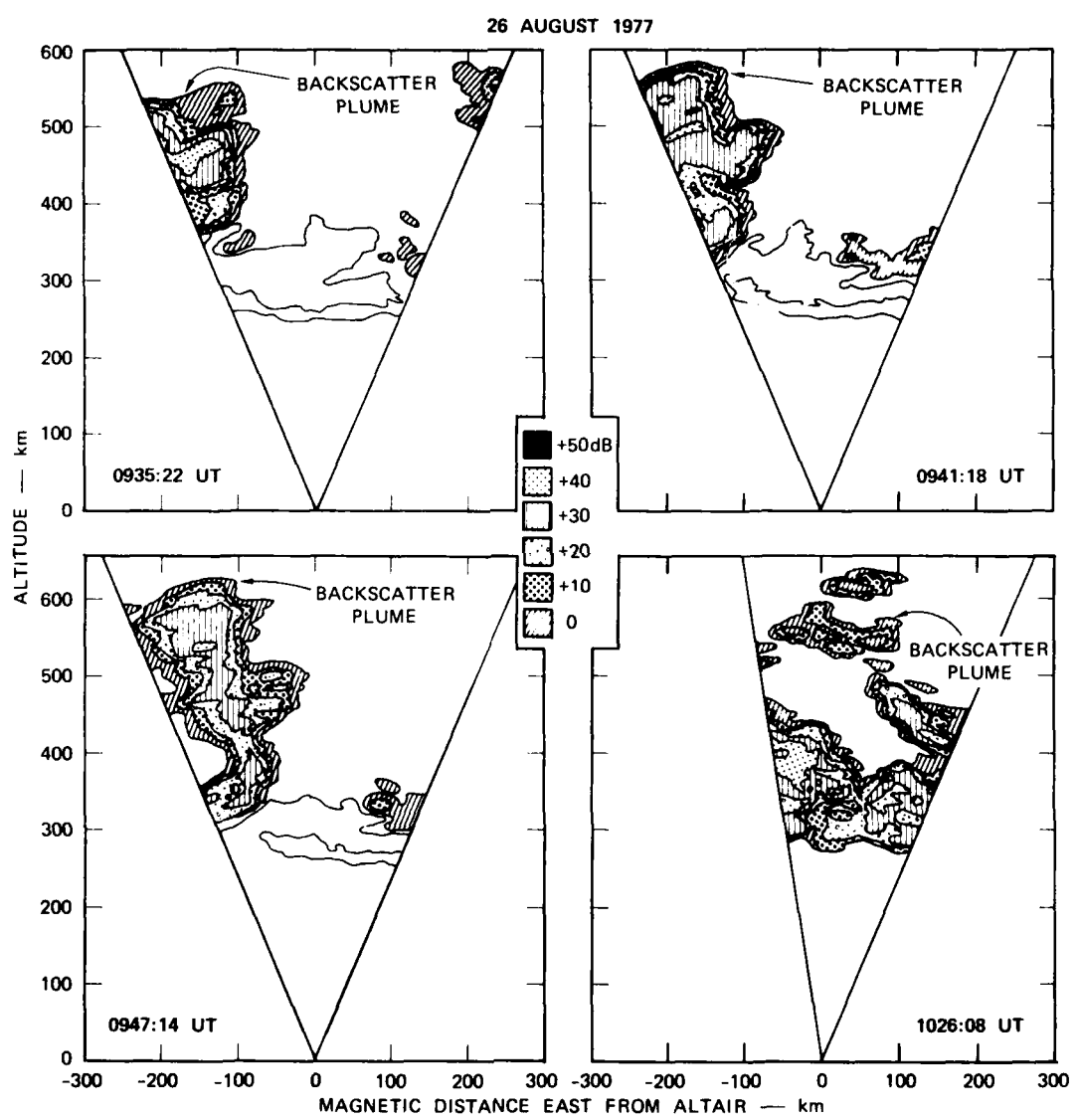


FIGURE 7 A SEQUENCE OF ALTAIR MAPS SHOWING PLUME DECAY--26 AUGUST 1977 (0935-1026 UT)

upward growth velocity can be estimated by scaling the altitude displacement of the plume top as a function of time. The plume is seen to have moved from 535 km to 580 km altitude in about 6 minutes, giving an upward velocity of 7.5 km/min, or 125 m/s. Despite this relatively large upward growth velocity, we see that the size of the peak backscatter region (40 dB) has shrunk slightly. That is, upward growth at this time is already associated with some decay in overall backscatter strength. The continued upward growth is seen by comparing the third map (0947:14 UT) to the first two. The top of the plume is seen to have reached 625 km altitude, giving the same upward velocity estimated earlier--125 m/s. The decay in backscatter strength, although present, is not rapid. Therefore, it seems that backscatter strength within plumes can stabilize or decay slightly even while the plume is still growing upward.

However, it is clear from the last map, taken at 1026:08 UT that the plume decayed significantly during this time interval. Comparing the strongest backscatter values within the plumes shown in the third and fourth maps, it appears that the decay rate was about 5 dB per 10 minutes. Comparing the top of the plume patches to the plume tops measured earlier, we estimate a mean upward velocity of 1.4 km/min, or 24 m/s. Therefore, the decay was also accompanied by a much reduced upward velocity.

The plume and bottomside-backscatter displacement as a function of time can be used to estimate their eastward and downward drift velocities. To estimate the eastward velocity, we used the second and third maps in Figure 7 because the high similarity in plume shapes allowed an accurate estimate of the displacement. From the two maps, we obtain an eastward drift velocity of 100 m/s. The vertical velocity was estimated from the displacement in the $10^5 \text{ e}1/\text{cm}^3$ contour along the bottomside of the F layer in the first and third maps. From these maps, we obtain a downward velocity of 20 m/s.

B. 8 August 1978 (1000-1100 UT)

In this second example, we examine how a plume decays as a function of time. The plume of interest entered the sector scanned by ALTAIR at 1001 UT. At that time, the top of the head of the plume was already at an altitude of 620 km. Upward growth continued until 1016 UT when the head reached an altitude of 680 km. The map showing peak plume development, which signifies the end of the generation phase and the beginning of the decay phase, is shown as the first map in Figure 8. A sequence of four other maps, taken later in time, which show the decay phase of the plume is also presented in Figure 8.

The start of plume decay is evident in the second map, taken 6 minutes later. The 40-dB contours within the plume have become patchy and there is only slow upward plume growth. In the third map, we see that the contours within the plume head have become detached from those in the neck. Furthermore, while the backscatter strength in the head has continued to decrease, that within the neck has increased slightly. The rejuvenation in backscatter strength in the neck corresponds with a slight expansion in the thickness of the bottomside backscatter and further development of a small plume to the west of the plume of interest.

In the last two maps in Figure 8, we see the continued decay and complete disappearance of the original plume head. The neck of the plume is seen to have weakened in the fourth map. By the time of the fifth map, the neck has also disappeared or has become much weaker, and any low-altitude remnant that might exist is outside the sector scanned by ALTAIR. The plume on the east side of the fifth map corresponds to the small plume seen in earlier maps (to the west of the plume of interest) that did not develop to nearly the size of the plume of interest. Bottomside backscatter is also seen to have finally weakened in the last map. To obtain an approximate decay rate of the plume, we estimate that the backscatter strength in the head decreased 10 dB in 5-1/2 minutes, or about 18 dB in 10 minutes. The decay rate between the third and fourth maps is also about 18 dB in 10 minutes.

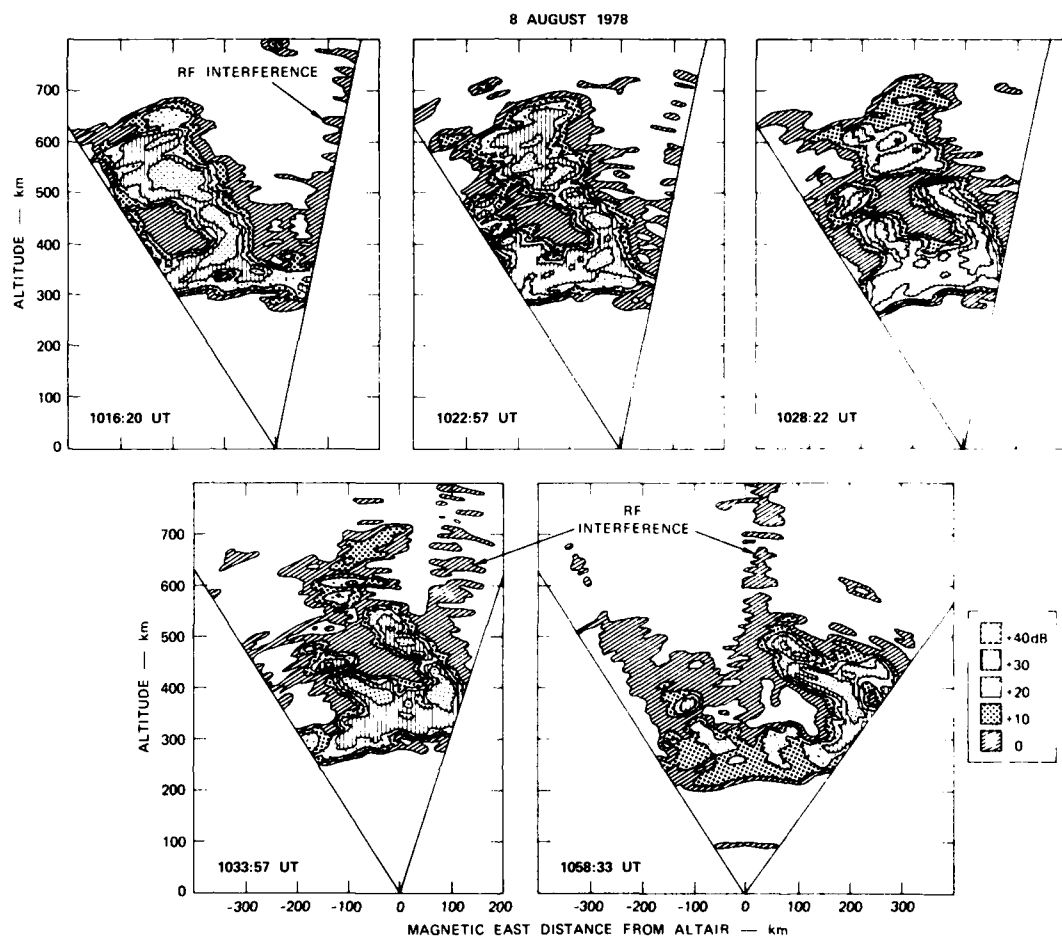


FIGURE 8 A SEQUENCE OF ALTAIR MAPS SHOWING PLUME DECAY--8 AUGUST 1978 (1000-1100 UT)

Finally, it is worth noting the horizontal and vertical velocities associated with plume transport. The eastward plume displacement seen in the second map relative to the first (first pair of maps) gives an eastward drift velocity of 150 m/s. The displacement between the second and third maps (second pair) gives a velocity of 157 m/s. The third pair of maps gives a velocity of 176 m/s. These estimates suggest an increasing velocity with time, or at least an average eastward velocity of about 160 m/s. The vertical velocity can be estimated by noting that bottomside backscatter has descended from 300 km altitude at 1016 UT to around 220 km at 1059 UT. Since we have found from other data sets (where IS data were available) that the descent of the bottomside backscatter is accompanied by a lowering of the F layer, we can use this displacement as an estimate of downward bulk plasma motion. Using the above values, we obtain a downward velocity of 31 m/s.

C. 1 August 1978 (1207-1237 UT)

In the second example, we described what we believe is a typical decay pattern for a plume. However, variations in this decay pattern are often seen, usually in the relative decay rates of the head and neck of the plume. Bottomside backscatter is usually the last to disappear. In this third example, we describe a decay pattern that is somewhat more complex than that described in the second example.

The backscatter maps of interest are shown in Figure 9. At 1207:40 UT, we see a plume that extended up to about 750 km. Without knowledge of the plume's time history, we cannot determine when the decay phase began. However, the fact that the strongest backscatter is seen below 550 km, apparently in the neck of the plume, and not in the head of the plume suggests that the decay phase is under way. In any case, decay of the plume is clearly evident in the following maps in Figure 9.

The plume structure in the first map is unusual in that the tilt of the plume appears to change from slightly west of vertical (which is typically seen) below 550 km altitude, to east of vertical above that altitude. This transition altitude is also significant in the way it

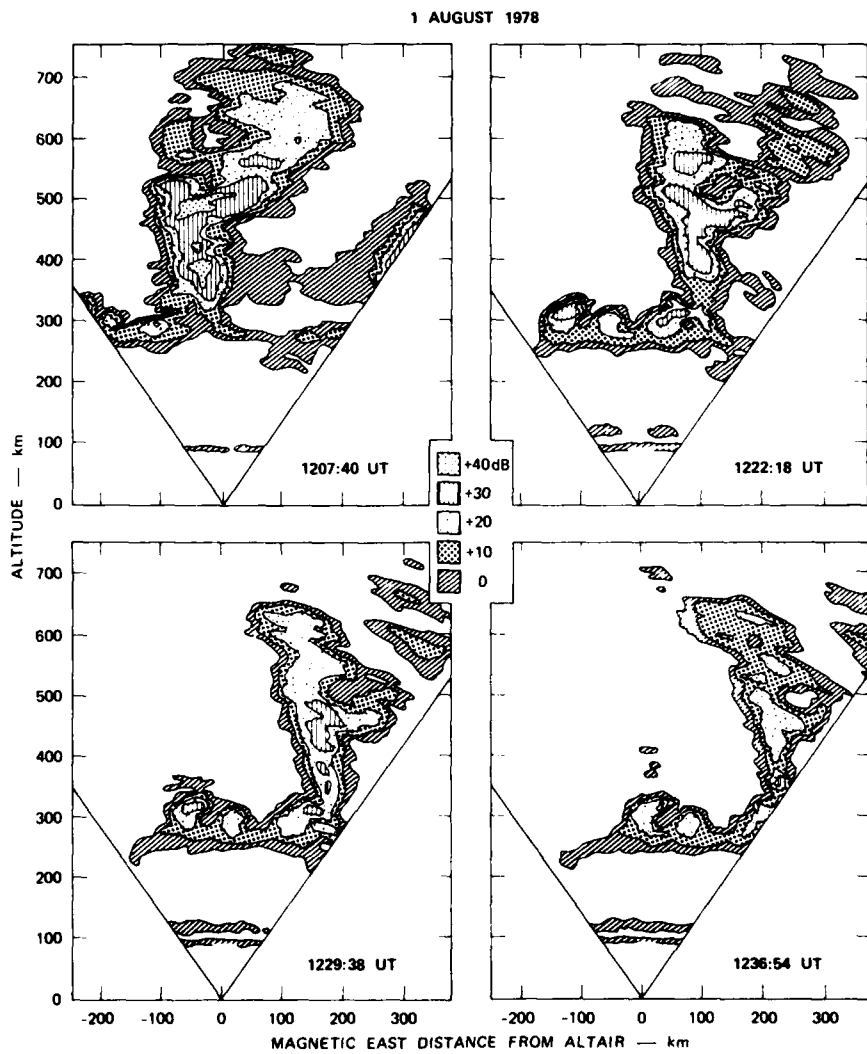


**FIGURE 9 A SEQUENCE OF ALTAIR MAPS SHOWING PLUME DECAY--
8 AUGUST 1978 (1207-1237 UT)**

segments the altitude distribution of backscatter strength. If we compare the altitude distribution of backscatter strength in this plume to that for the plume shown in Figure 2 (at 0848:09 UT), we might be tempted to infer that the F-layer peak was located around 550 km. However, by examining electron-density profiles obtained in regions without backscatter from FAI, we found that the F-layer peak was located closer to 375 km altitude and that 550 km appeared to correspond to an altitude above which there is a drastic decrease in topside electron density. Therefore, the strong backscatter region (> 30 dB) that occurred within the plume segment having a westward tilt appears to coincide with a region of the surrounding F layer where the electron density was substantial. And, the weaker backscatter region that occurred within the plume segment having an eastward tilt appears to correspond with a region well above the peak of the surrounding F layer where the electron density was much more tenuous.

In the second map, taken 14 minutes after the first map, the plume is seen to have decayed in peak backscatter strength by about 10 dB. The high-altitude portion of the plume has become patchy, and backscatter within the entire plume has become generally weaker. However, in the midst of this general decay process, we see that the west portion of the high-altitude plume segment has actually increased in strength. If we look at the following maps, it appears as if the enhancement in the high-altitude segment is actually a continued upward growth of the lower portion of the plume. This interpretation is based on the fact that the extension into the high-altitude portion occurs directly in line with the low-altitude segment, including a westward tilt. There is also a 10-dB increase in bottomside backscatter strength, which is interpreted to indicate that there are still generation conditions for 1-m FAI in the bottomside F layer.

The continued decay of the plume is seen in the following two maps, corresponding to scans made at 1229:38 and 1236:54 UT. If we compare the plumes in the last two maps, we find that the peak plume backscatter has decreased by approximately 10 dB in 14-1/2 minutes, identical to the decay found in the first two maps. Therefore, we obtain an approximate decay

rate of 7 dB per 10 minutes for this event. Finally, we note from the last two maps that the bottomside backscatter has entered into a decay phase. We find that the bottomside backscatter region has stopped growing around 1230 UT, and began to weaken by 1237 UT.

As in the previous example, we note the horizontal and vertical velocities associated with the plume. Taking the maps in pairs and using the relative plume displacements, we obtain an average eastward drift velocity of 150 m/s. And using the displacement of bottomside backscatter, we obtain a downward velocity of 9 m/s.

D. Summary of Decay-Phase Characteristics

From the three examples, we have found that the following plume characteristics appear during the decay phase:

- (1) Plumes begin to decay around the time they approach their maximum height. Or, plumes begin their decay phase when the plume growth velocity begins to decrease.
- (2) Plumes can have decay rates of 5 to 18 dB per 10 minutes.
- (3) Decay rates appear to be faster in the topside than in the bottomside F layer. In fact, it is possible to have growth conditions in the bottomside occurring simultaneously with decay conditions in the topside F layer. The converse seems to occur much less frequently, although an example of this kind was shown in Figure 2.
- (4) The velocity of eastward plume drift during the decay phase is similar to that found during the growth phase--on the order of 100 to 150 m/s.
- (5) During the decay phase, the altitude of bottomside backscatter decreases at a rate of 10 to 30 m/s. This velocity is believed to be associated with the lowering of the F layer.

V DISCUSSION AND CONCLUSIONS

In the preceding sections, we have shown that a number of characteristics regarding the time evolution of backscatter plumes can be extracted from time sequences of backscatter maps obtained with a steerable backscatter radar. Characteristics from both the growth and decay phases were described, some that have never before been reported, and others verifying earlier results. In this section, we review these plume characteristics and discuss their implications in terms of the Rayleigh-Taylor instability and other potential sources for these characteristics.

A. Initial Conditions for Plume Development

We have shown that plumes appear to originate in the bottomside of the F layer and to be associated with local elevations in bottomside backscatter. Furthermore, we have shown that plumes, developing in the bottomside F layer, are spatially collocated with localized plasma depletions, or bubbles. If we interpret the altitude-modulated bottomside backscatter as a tracer for a bottomside F layer that is similarly modulated, these observations would be consistent with the concept that altitude modulation of the bottomside F layer is associated with the development of a plasma bubble, as suggested by Woodman and La Hoz (1976) and simulated numerically by Scannapieco and Ossakow (1976).

The occurrence of altitude modulation of the bottomside F layer was shown by Weber et al. (1978). They used an airborne all-sky spectrophotometer and an ionosonde to show that 6300 Å airglow depletions in the nighttime equatorial ionosphere result from local elevations in the bottomside F layer. The airglow depletions were found to be north-south-aligned, extending more than 1200 km in north-south direction and 50-to-200 km in east-west direction. They proposed that these airglow depletions might be bottomside F-layer signatures of plasma bubbles. The east-west scale sizes of airglow depletions agree very well with the

corresponding scale sizes of plasma bubbles measured by in-situ probes (Hanson and Sanatani, 1973; McClure et al., 1977), and of backscatter plumes measured by ALTAIR. As shown by Scannapieco and Ossakow (1976), the most probable plasma-bubble size is the scale size of the initial electron-density perturbations, particularly during the generation phase.

For the moment, let us assume that we have such an altitude modulation without questioning what the modulation source of the bottomside F layer might be. Consider the spatial distribution of plasma irregularities that would develop under three conditions: (1) the post-sunset rise of the F layer, (2) a high F layer that is susceptible to the Rayleigh-Taylor instability, and (3) an eastward neutral wind. The first and second cases have been considered in several theoretical models of equatorial spread F (e.g., Ossakow et al., 1979).

An upward-moving F layer that is moving rapidly will become unstable along its bottomside plasma-density gradient via the gradient-drift instability (e.g., Linson and Workman, 1970). Its nonlinear development should also give rise to plasma bubbles. Consider its effectiveness at generating irregularities during the post-sunset rise of the F layer. For example, at a 300 km altitude, a velocity of 37 m/s (for a gradient scale length of 10 km) will result in a growth e-folding time of 5 minutes. That is, the amplitude of irregularities would increase by a factor of 2.7 in five minutes. (In comparison, the equivalent "gravitational velocity" for the Rayleigh-Taylor instability is 14 m/s. This velocity results in a growth rate that is just above the threshold of growth.) Because velocities as high as 50 m/s occur during the post-sunset rise of the F layer (Woodman, 1970), the gradient-drift instability will contribute to the generation of irregularities and plumes.

Let us now consider the effects of an altitude-modulated F layer on irregularity generation. A contour representation of such an F layer is shown in Figure 10(a). The coordinates are altitude (upward) and horizontal (magnetic east-west) distance. For simplicity, we assume that the electron-density gradient, ∇N , varies in direction but has a fixed scale length. We are interested in the spatial distribution of irregularity

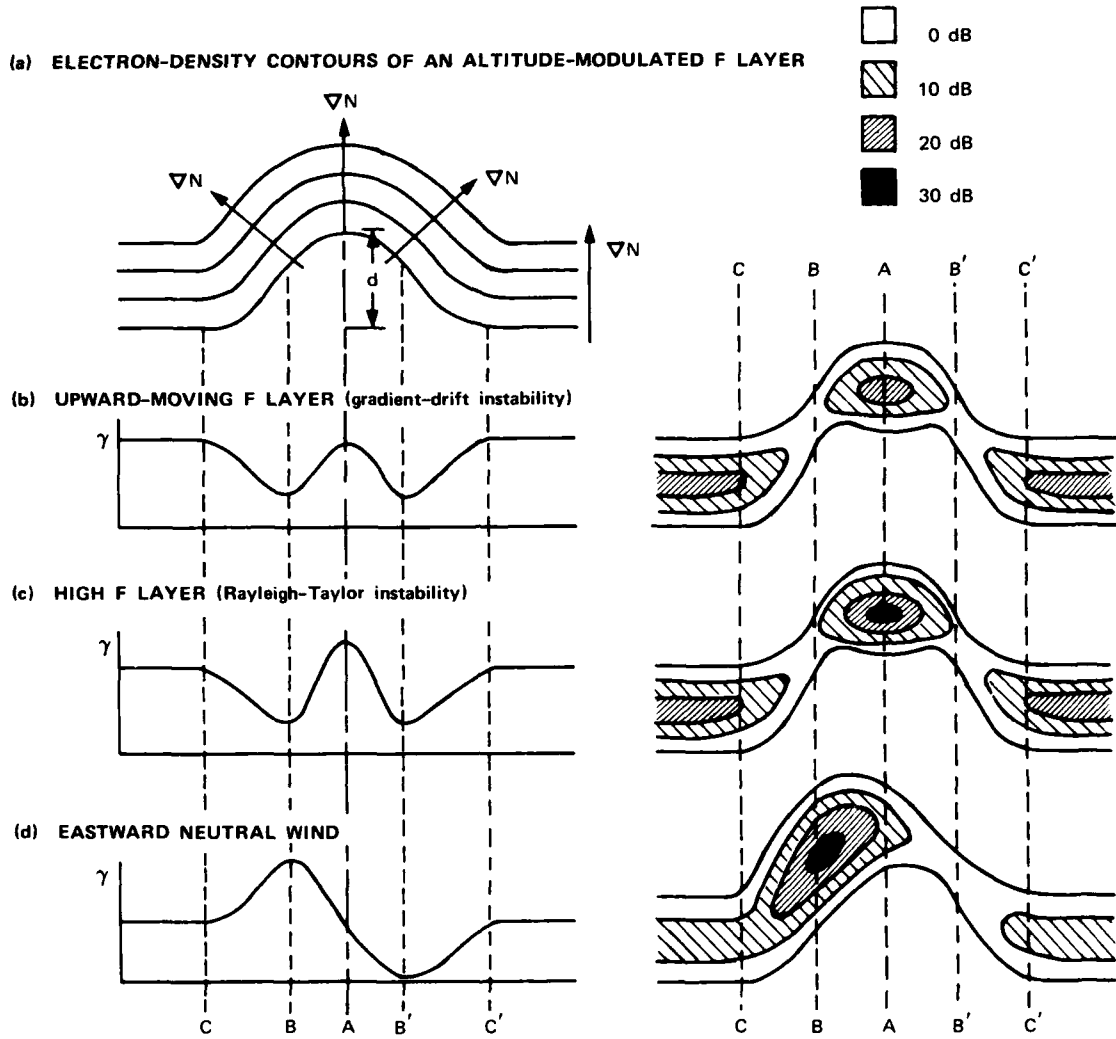


FIGURE 10 SPATIAL DISTRIBUTION OF GROWTH RATE AND BACKSCATTER STRENGTH PRODUCED BY (a) AN UPWARD-MOVING F LAYER, (b) A HIGH F LAYER, AND (c) AN EASTWARD NEUTRAL WIND

strength about the axis of symmetry, A, which is shown aligned with the location of maximum elevation in the electron density contours.

For a given equivalent velocity vector, the linear growth rate, γ , is proportional to the component of the electron-density gradient that is in the direction of the velocity vector. On this basis, we can determine the growth rate along the bottomside of the F layer as a function of horizontal distance. The growth-rate variation for the case of an

upward-moving F layer is shown on the left side of Figure 10(b). Because the velocity vector is directed upward, the growth rate is maximum outside the region CC' and at the axis of symmetry, A--i.e., in regions where the electron-density gradient is also directed upward. Minima in growth rate occur at B and B', where the upward component of electron density gradient is smallest.

Assuming that the largest linear growth rate leads to the largest amplitude FAI, and hence to the strongest backscatter, the corresponding contour plot of bottomside backscatter is shown on the right side of Figure 10(b). The point to note is that the backscatter strength contours are symmetrically distributed about A.

When the F layer is high, the equivalent gravitational velocity will be large and the Rayleigh-Taylor instability can replace the gradient-drift instability as the dominant source of FAI generation. But since the equivalent gravitational velocity vector is also directed upward, the spatial distribution of both growth rate and backscatter strength remain the same, as was shown in Figure 10(b).

Recalling that the linear growth rate is also proportional inversely to the ion-neutral collision frequency, we can expect a variation in the in the spatial distribution in Figure 10(b) if the depth of the altitude modulation, d, is of the order of a scale height of the neutral gas. (Indeed, in the examples presented the depth of modulation was found to range from 30 to 60 km, which is of the order of the scale height of the nighttime equatorial atmosphere.) In this case, we would expect a significantly larger growth rate (e.g., Ossakow and Chaturvedi, 1978) in the elevated region. This situation is depicted in Figure 10(c) by the peak in both growth rate and backscatter strength at the axis of symmetry. The depth of the minima (at B and B') will depend on the extent to which the increasing height of the F layer offsets the decreasing vertical component of the electron density gradient. But as in the first case, the spatial distribution of backscatter strength is symmetric about A.

Now consider the third case [Figure 10(d)], in which there is an eastward neutral wind. Rishbeth (1971) has shown theoretically that the degree to which the F-region plasma is coupled to the neutral wind depends on the ability of the E-region conductivity to short-circuit the development of a downward-directed polarization electric field. At night, the E-region conductivity decreases so that the polarization field can build up to produce an eastward plasma drift. However, because the E-region conductivity remains finite, the F-region plasma drift velocity is smaller than the neutral-wind velocity (Woodman, 1972). Therefore, in the moving frame of the plasma, we still have an eastward neutral wind, or equivalently, an upward-directed electric field in the reference frame of the neutral wind.

The combined presence of an eastward neutral wind and an upward-moving (or high) F layer results in a plasma-drift velocity vector (in the reference frame of the neutral wind) that is directed westward and upward. The observation that backscatter plumes tilt westward of vertical has been attributed to the presence of this kind of plasma-drift velocity vector (Woodman and La Hoz, 1976; Ott, 1978; Ossakow and Chaturvedi, 1978). In examining the electron-density contours and corresponding directions of the electron-density gradient in Figure 10(a), it is clear that the maximum growth rate will occur on the west wall of the elevated region, where the electron-density gradient is most closely aligned with the velocity vector. The spatial distribution of growth rate and the corresponding backscatter strength, for this case, is shown in Figure 10(d).

In Figure 10(d), the backscatter strength outside the sector CC' will depend on the vertical component of the plasma drift velocity. In the vicinity of B, backscatter strength will be enhanced, with the maximum located where the plasma-drift velocity vector is most closely aligned with the plasma-density gradient. And in the vicinity of B', the backscatter strength should be very small (if not zero) because the plasma-drift velocity vector is directed nearly perpendicular to the plasma-density gradient. The spatial distribution of backscatter strength shown in Figure 10(d) closely resembles the backscatter pattern shown in Figure 3. Plume growth from the enhanced backscatter region would

produce a backscatter pattern similar to those presented in Figures 3, 4, 7, and 9. And as described in Section III-B, this pattern of plume growth resembles the "C-shaped" and "fishtail" patterns found in Jicamarca radar RTI displays of 50-MHz backscatter (Woodman and La Hoz, 1976).

From the above discussion, it seems likely that the eastward neutral wind is a source of the east-west asymmetry found in backscatter patterns. Furthermore, because the west wall of the elevated region is the most unstable region, it is the region in which plumes are most likely to develop. Therefore, the combined occurrence of altitude modulation (in the F-layer electron-density contours) and the presence of an eastward neutral wind seems to be a likely candidate for a "seed" mechanism that controls the patchy and sporadic nature of backscatter plume development.

As further support for this concept, we point to another source mechanism that might enhance the effects just described. Perkins and Doles (1975) showed that the gradient-drift instability--the mechanism believed to produce striations in barium ion clouds--is damped whenever there is an electric field component parallel to the plasma-density gradient. That is, the growth rate as determined from the plasma-density gradient and the perpendicular component of the electric field is suppressed by the presence of a parallel electric field component. The quenching effect is apparently produced by the velocity shear that must develop in the plasma-density gradient region as a result of trying to maintain current continuity. If this velocity shear mechanism is operative in the equatorial F layer, we can envision suppression of backscatter strength in all regions except B in Figure 10(d).

The role of the eastward neutral wind in establishing a proper alignment between plasma drift velocity and plasma-density gradient can be extremely important in explaining several puzzling questions. For example, what is the source of day-to-day variability in spread-F occurrence? Is there a seed mechanism that initiates the development of backscatter plumes?

The day-to-day variability of spread-F occurrence could be attributed to the variability in (1) the eastward neutral wind, (2) the effective

upward plasma velocity, and (3) the direction of the local plasma-density gradient. To further complicate matters, the above-mentioned factors are coupled during the post-sunset period. The lifting of the F layer results in reduced ion drag, thereby accelerating the neutral gas (Anderson and Roble, 1974). And, as discussed later, the large-scale tilt angle of the bottomside F layer during this period depends on the upward plasma velocity. Therefore, variability in the post-sunset rise velocity of the F layer (Woodman, 1970) will also be reflected in the neutral wind and the tilt angle of the plasma density gradient. It is possible that the phasing of these coupled effects would determine the magnitude of the resultant variability in spread-F occurrence.

An interesting complication is the observation in the second example in Section III that the altitude modulation did not appear to move eastward at the same speed as that of the plumes. In this case, the relative velocity between the plasma and the neutral wind becomes that of the neutral wind as measured in the corotating frame of the earth (e.g., Sipler and Biondi, 1978), as much as a few hundred meters per second. Furthermore, if the east-west transport of the altitude-modulated region is independent of the eastward plasma drift, we do not have to be overly concerned with the phasing requirements of acceleration of the neutral wind by a rising F layer and the westward acceleration of the F-region plasma by the F-region dynamo. Depending on the frequency of occurrence of this kind of event, the east-west transport velocity of the altitude-modulated region might be of vital importance in determining the effectiveness of the seed mechanism.

The importance of the eastward neutral wind in plasma-bubble generation has recently been proposed by Chiu and Straus (1979). However, they showed that the eastward neutral wind is effective in the region between the E and F layers where the ion-neutral collisions are much more frequent than in the nighttime F layer. They did not consider the presence of horizontal gradients in electron density.

B. Growth Velocity of Backscatter Plumes

We have shown that plumes develop upward from the bottomside into the topside of the F layer with velocities between 125 and 350 m/s. These velocities compare very favorably with ion flow velocities of up to 250 m/s measured within plasma bubbles (McClure et al., 1977), and with Doppler spectral measurements made by other backscatter radars from equatorial FAI. Doppler measurements showed vertical velocities that were often greater than 200 m/s (McClure and Woodman, 1972; Woodman and La Hoz, 1976; Kelley et al., 1976).

Bubble rise velocities have also been estimated theoretically using two-dimensional models of the Rayleigh-Taylor instability (Scannapieco and Ossakow, 1976; Ossakow and Chaturvedi, 1978; Ott, 1978). Ossakow and Chaturvedi (1978) showed that bubble rise velocities around 100 to 300 m/s can be reached if the bubble altitude is above 400 km and if the percentage depletion is very high. These theoretical predictions appear to agree with observations.

However, care must be taken in the interpretation of these measured plume-growth velocities. Because the examples selected were taken from a time period when the post-sunset rise of the F layer takes place, the $E \times B$ velocity due to the background eastward electric field must be subtracted from the measured velocities. Although we do not have estimates of the eastward electric field for the examples presented, we do know that the upward electrodynamic drift of the F layer is no more than about 50 m/s (Woodman, 1970). Therefore, we can at least interpret the measured velocities as upper-bound values for bubble velocities. Smaller bubble velocities simply mean that the percentage depletion need not be as high.

The importance of the eastward electric field (i.e., an upward-moving F layer) was pointed out by Anderson and Haerendel (1979). Using flux-tube-integrated values of electron density and Pedersen conductivity, they showed that without an eastward electric field it takes more than an hour for a plasma bubble to reach an upward velocity of 200 m/s. On the other hand, with an eastward electric field of 0.6 mV/m (or a plasma

drift velocity of 24 m/s), they showed that the bubble rise velocity reached 200 m/s in tens of minutes. These theoretical estimates of the time it takes for a bubble to reach 200 m/s appear to be in reasonable agreement (although on the long side) with the examples presented in this paper. Plume (or equivalently, plasma bubble) formation was found to occur in less than 6 minutes with an associated mean upward velocity on the order of 200 m/s. However, it is likely that the times predicted for the bubble velocity to reach 200 m/s can be made to agree with the times of plume formation if the effects of an eastward neutral wind (and perhaps a larger eastward electric field) are included.

We note, however, that the F layer reverses its upward motion within an hour or two after local sunset, and this downward motion is associated with a westward electric field. Plumes that develop under these conditions would be predicted by Anderson and Haerendel (1979) to have growth characteristics different than those described in Section III. Because the westward electric field would act in opposition to the gravitational velocity, the time for upward plume growth would be much longer than those found near F-region sunset. The vertical electric field produced by the eastward neutral wind would also act to damp out irregularity growth. This might be a reason for not observing plume generation in ALTAIR data taken later at night. Measurable growth probably takes place in a time period long compared to the time of observation.

A feature of considerable interest and one that is implicit in the structure of this report (i.e., division into a growth and decay phase) is the altitude stagnation of backscatter plumes, and presumably plasma bubbles. The completion of the growth phase of plumes (and bubbles) is defined by the slowdown and ultimate end to their upward growth. The fact that plumes begin to dissipate at that point is understandable in terms of the Rayleigh-Taylor or gradient-drift instability. Without upward velocity, the instability does not continue to maintain the electron-density gradients necessary to drive other instabilities that produce the small-scale FAI. However, the question of interest is, why do the plumes or bubbles drastically decrease upward movement, even at altitudes where theory predicts rapid upward movement?

Tsunoda (1980b) examined ALTAIR data taken during a latitude scan and noted this apparent altitude stagnation of a plasma bubble (and associated backscatter plume). He found that the seemingly small upward velocity was consistent with model predictions by Anderson and Haerendel (1979), which include the use of (1) flux-tube-integrated values of electron density and Pedersen conductivity, and (2) the nonuniform latitudinal distribution of electron density produced by the evening enhancement of the equatorial anomaly. In other words, the smallness of the upward velocity was produced by a westward electric field, which plays a more dominant role in a model that includes flux-tube-integration and the presence of an equatorial anomaly. Therefore, a source that might initiate a decay phase would be the reversal of the eastward electric field to a westward direction. However, until we determine the local time behavior of plume decay, it is difficult to ascertain whether altitude stagnation results from this reversal or whether there are other factors involved.

Finally, on the subject of plume growth, we have shown that new plumes can develop in the vicinity of old plumes. And, during the generation phase of the new plume, we found that the old plume showed no signs of regeneration and that it continued its decay phase. The fact that plumes can grow independently of one another supports the concept that plumes (or bubbles) are generated in the bottomside F layer and, once "launched," become independent of the generation conditions. This characteristic strongly supports the nonlinear development of bubbles via the Rayleigh-Taylor instability.

C. Backscatter Strength of Plumes

We have shown that plume backscatter strength increases during upward plume growth, regardless of whether the plume head is in the bottomside or topside of the F layer. Backscatter appears to stabilize in strength around the time upward plume growth ceases, and appears to decay thereafter. These plume observations appear to be consistent with plasma bubble models based on the Rayleigh-Taylor instability, in that these models predict development of stronger irregularities with upward bubble

movement. The theoretical models, however, do not predict a slowdown in upward bubble movement (see previous subsection). Of course, if the bubble is halted for any reason, irregularity growth is expected to stop and be followed by a decay phase.

We have shown that plumes can decay at a rate of 5 to 18 dB in 10 minutes. This estimate suggests that the strongest backscatter plume, which might have a strength of 50 dB above IS, would decay completely in 70 to 100 minutes. A more typical plume (30 dB above IS) would disappear in 43 to 60 minutes. These decay rates are comparable to other estimates of the lifetime of equatorial irregularities. Backscatter patches observed with radars at 18 and 27.8 MHz were found to have a mean lifetime of 20 minutes (Clemesha, 1964; Kelleher and Skinner, 1971). The lifetimes of equatorial irregularities that support non-great-circle transequatorial propagation paths at HF frequencies range from 5 to 60 minutes with a median value of 20 minutes (Rottger, 1973). The estimated lifetimes, of course, depend on the sensitivity and dynamic range of the radar systems employed. We should also point out that the lifetimes of these smaller-scale FAI appear to be much shorter than the larger-scale FAI responsible for equatorial scintillations of radio signals (Basu et al., 1978).

The decay of backscatter plumes appears to be real in that it commences around the time the plume reaches maximum height. However, care should be taken in the interpretation of decay rates because there is a possibility that backscatter from 1-m FAI is aspect-dependent. That is, stronger backscatter might be observed when the radar beam is directed west of vertical than when it is directed east of vertical. A possible reference direction might be the plasma density gradient. Evidence for the possible presence of aspect dependence was found at HF frequencies. Backscatter measurements by Clemesha (1964) and Kelleher and Skinner (1971) were found to maximize in the westerly directions. If aspect dependence is a factor at VHF, the decay rates found in the examples (Section IV) would have to be reduced.

D. A Working Model of Plume Growth and Decay

On the basis of results presented in this report, plumes appear to have the following life cycle. Plumes are initiated around the time of F-layer sunset, during the post-sunset rise of the F layer. Their times of observations are determined by the growth conditions described by Anderson and Haerendel (1979) and by the effectiveness of the seed mechanism. The growth phase takes approximately one hour, and the decay phase perhaps a little longer--say, two hours. Therefore, a plume generated around 2000 LT (local time) will have dissipated by 2300 LT. Typically, the post-sunset rise of the F layer lasts for an hour (Woodman, 1970). The cutoff time, therefore, for plume observation would be extended to about local midnight. This time period for plume occurrence is consistent with ALTAIR observations and the conclusions drawn by Basu et al. (1978) that small-scale (i.e., meter-scale) FAI are usually absent after local midnight.

The conduciveness of the time of the post-sunset rise of the F layer to plume generation is established by both a large-scale tilt (many hundreds of kilometers) and a local, altitude-modulated region in the bottom-F layer. The large-scale tilt is produced by the post-sunset rise of the F layer immediately after the passage of the solar terminator. The westward velocity of the solar terminator is $15^\circ/\text{hr}$, or 27.75 km/min . Therefore, the large-scale tilt extends from the location of the solar terminator 1665 km to the east. The bottomside gradient of the F layer in this sector will be tilted west of vertical by the ratio of the upward velocity to the velocity of the solar terminator, or about 6° . To the east of this sector, the tilt of the bottomside F layer is in the opposite sense because the F layer there is descending. Consequently, in the presence of an eastward neutral wind, the westward tilt in the bottomside F layer will tend to reduce the damping effects of the velocity-shear mechanism (Perkins and Doles, 1975) or irregularity growth, whereas the eastward tilt will tend to enhance this damping effect. Although this large-scale eastward tilt does not exclude the generation of plumes in sector, the tilt would tend to stunt their growth.

Local, altitude-modulated regions in the bottomside F layer act together with the large-scale tilts to provide a means of satisfying the orthogonal vector relationship between the electric field and plasma-density gradient. Because the angular response of this directional filter contributes to the characteristics of the observed plume-growth characteristics, it is important to establish the characteristics of the velocity-shear mechanism. Another area of research is the source and characteristics of the altitude modulation. Are they due to gravity waves? Do their occurrence characteristics contribute to the variability in occurrence of spread F?

Once the plumes (and plasma bubbles) are initiated, the growth characteristics are primarily controlled by the strength and direction of the electric field vector. At high altitudes, the gravitational velocity becomes significant and must be accounted for. Altitude stagnation could be the result the opposing contributions by a westward electric field and the gravitational velocity, the percentage depletion of the plasma bubble, or an as yet undetermined mechanism.

REFERENCES

- Anderson, D. N. and G. Haerendel, "The Motion of Depleted Plasma Regions in the Equatorial Ionosphere," J. Geophys. Res., Vol. 84, p. 4251, 1979.
- Anderson, D. N. and R. G. Roble, "The Effect of Vertical E × B Ionospheric Drifts on F Region Neutral Winds in the Low-Latitude Thermosphere," J. Geophys. Res., Vol. 79, 5231, 1974.
- Balsley, B. B., G. Haerendel, and R. A. Greenwald, "Equatorial Spread-F: Recent Observations and a New Interpretation," J. Geophys. Res., Vol. 77, p. 5625, 1972.
- Basu, S., S. Basu, J. Aarons, J. P. McClure, and M. D. Cousins, "On the Coexistence of Kilometer- and Meter-Scale Irregularities in the Nighttime Equatorial F Region," J. Geophys. Res., Vol. 83, p. 4219, 1978.
- Bibl, K., B. W. Reinisch, and S. Smith, "Equatorial Spread-F Observations during August 1977 at Kwajalein, M.I.," University of Lowell, Lowell, MA, 1977.
- Chiu, Y. T. and J. M. Straus, "Rayleigh-Taylor and Wind-Driven Instabilities of the Nighttime Equatorial Ionosphere," J. Geophys. Res., Vol. 84, p. 3283, 1979.
- Clemesha, B. R., "An Investigation of the Irregularities in the F-Region Associated with Equatorial Type Spread-F," J. Atmos. Terr. Phys., Vol. 26, p. 91, 1964.
- Farley, D. T., B. B. Balsley, R. F. Woodman, and J. P. McClure, "Equatorial Spread F: Implications of VHF Radar Observations," J. Geophys. Res., Vol. 75, p. 7199, 1970.
- Hanson, W. B. and S. Sanatani, "Large Ni Gradients Below the Equatorial-F Peak," J. Geophys. Res., Vol. 78, p. 1167, 1973.
- Haerendel, G., "Theory of Equatorial Spread F," preprint, Max-Planck-Institut für Physik and Astrophysik, Institut für extraterrestrische Physik, 8046 Garching, FRG, 1974.
- Hudson, M. K. and C. F. Kennel, "Linear Theory of Equatorial Spread F," J. Geophys. Res., Vol. 80, p. 4581, 1975.

- Kelley, M. C., G. Haerendel, H. Kappler, A. Valenzuela, B. B. Balsley, D. A. Carter, W. L. Ecklund, C. W. Carlson, B. Hausler, and R. Torbert, "Evidence for a Rayleigh-Taylor Type Instability and Upwelling of Depleted Density Regions During Equatorial Spread-F," Geophys. Res. Letts., Vol. 3, p. 448, 1976.
- Kelleher, R. F. and N. J. Skinner, "Studies of F Region Irregularities at Nairobi. II-By Direct Backscatter at 27.8 MHz," Ann. Geophys., Vol. 27, p. 195, 1971.
- Linson, L. M. and J. B. Workman, "Formation of Striations in Ionospheric Plasma Clouds," J. Geophys. Res., Vol. 75, p. 3211, 1970.
- McClure, J. P. and R. F. Woodman, "Radar Observations of Equatorial Spread F in a Region of Electrostatic Turbulence," J. Geophys. Res., Vol. 77, p. 5617, 1972.
- McClure, J. P., W. B. Hanson, and J. H. Hoffman, "Plasma Bubbles and Irregularities in the Equatorial Ionosphere," J. Geophys. Res., Vol. 82, p. 2650, 1977.
- Morse, F. A., B. C. Edgar, H. C. Koons, C. J. Rice, W. H. Heikkila, J. H. Hoffman, B. A. Tinsley, J. D. Winningham, A. B. Christensen, R. F. Woodman, J. Pomalaza, and N. R. Teixeira, "Equion, An Equatorial Ionospheric Irregularity Experiment," J. Geophys. Res., Vol. 82, p. 578, 1977.
- Ossakow, S. L. and P. K. Chaturvedi, "Morphological Studies of Rising Equatorial Spread F Bubbles," J. Geophys. Res., Vol. 83, p. 2085, 1978.
- Ossakow, S. L., S. T. Zalesak, B. E. McDonald, P. K. Chaturvedi, "Nonlinear Equatorial Spread F: Dependence on Altitude of the F Peak and Bottomside Background Electron Density Gradient Scale Length," J. Geophys. Res., Vol. 84, p. 17, 1979.
- Ott, E., "Theory of Rayleigh Taylor Bubbles in the Equatorial Ionosphere," J. Geophys. Res., Vol. 83, p. 2066, 1978.
- Perkins, F. W. and J. H. Doles III, "Velocity Shear and the $E \times B$ Instability," J. Geophys. Res., Vol. 80, 211, 1975.
- Rishbeth, H., "Polarization Fields Produced by Winds in the Equatorial F-Region," Planet. Space Sci., Vol. 19, p. 357, 1971.
- Rottger, J., "Wave-Like Structures of Large-Scale Equatorial Spread-F Irregularities," J. Atmos. Terr. Phys., Vol. 35, p. 1195, 1973.
- Scannapieco, A. J. and S. L. Ossakow, "Nonlinear Equatorial Spread-F," Geophys. Res. Letts., Vol. 3, p. 451, 1976.

- Sipler, D. P. and M. A. Biondi, "Equatorial F-Region Neutral Winds from Nightglow OI 630.0 NM Doppler Shifts," Geophys. Res. Letts., Vol. 5, p. 373, 1978.
- Towle, D. M., "VHF and UHF Radar Observations of Equatorial Ionospheric Irregularities and Background Densities," accepted for publication, Radio Science, 1979.
- Tsunoda, R. T., "On the Spatial Relationship of 1-Meter Equatorial Spread-F Irregularities and Plasma Bubbles," in press, J. Geophys. Res., 1980a.
- Tsunoda, R. T., "Magnetic-Field-Aligned Characteristics of Plasma Bubbles in the Nighttime Equatorial Ionosphere," Submitted to J. Atmos. Terr. Phys., 1980b.
- Tsunoda, R. T. and D. M. Towle, "On the Spatial Relationship of 1-Meter Equatorial Spread-F Irregularities and Depletions in Total Electron Content," Geophys. Res. Letts., Vol. 6, p. 873, 1979.
- Tsunoda, R. T., M. J. Baron, J. Owen, and D. M. Towle, "ALTAIR, An Incoherent-Scatter Radar for Equatorial Spread-F Studies," Radio Science, Vol. 14, p. 1111, 1979.
- Weber, E. J., J. Buchau, R. H. Eather, and S. B. Mende, "North-South Aligned Equatorial Airglow Depletions," J. Geophys. Res., Vol. 83, p. 712, 1978.
- Woodman, R. F., "Vertical Drift Velocities and East-West Electric Fields at the Magnetic Equator," J. Geophys. Res., Vol. 75, p. 6249, 1970.
- Woodman, R. F., "East-West Ionospheric Drifts at the Magnetic Equator," Space Res. XII, Vol. 12, p. 969, 1972.
- Woodman, R. F. and C. La Hoz, "Radar Observations of F-Region Equatorial Irregularities," J. Geophys. Res., Vol. 81, p. 5447, 1976.

DISTRIBUTION LIST

DEPARTMENT OF DEFENSE

Assistant Secretary of Defense
Comm., Cmd., Cont., & Intell.
ATTN: C3IST&CCS, M. Epstein
ATTN: Dir. of Intelligence Systems, J. Babcock

Assistant to the Secretary of Defense
Atomic Energy
ATTN: Executive Assistant

Command & Control Technical Center
ATTN: C-312, R. Mason
ATTN: C-650, G. Jones
3 cy ATTN: C-650, W. Heidig

Defense Advanced Rsch. Proj. Agency
ATTN: TIO

Defense Communications Agency
ATTN: Code 101B
ATTN: Code 480
ATTN: Code 810, J. Barna
ATTN: Code 205
ATTN: Code 480, F. Dieter

Defense Communications Engineer Center
ATTN: Code R123
ATTN: Code R720, J. Worthington
ATTN: Code R410, J. McLean
ATTN: Code R410, R. Craighill

Defense Intelligence Agency
ATTN: DB-4C, E. O'Farrell
ATTN: DC-7D, W. Wittig
ATTN: DT-1B
ATTN: DB, A. Wise
ATTN: DT-5
ATTN: HQ-TR, J. Stewart

Defense Nuclear Agency
ATTN: STVL
3 cy ATTN: RAAE
4 cy ATTN: TITL

Defense Technical Information Center
12 cy ATTN: DD

Field Command
Defense Nuclear Agency
ATTN: FCPR

Field Command
Defense Nuclear Agency
Livermore Division
ATTN: FCPR

Interservice Nuclear Weapons School
ATTN: TTV

Joint Chiefs of Staff
ATTN: C3S, Evaluation Office
ATTN: C3S

Joint Strat. Tgt. Planning Staff
ATTN: JLTW-2
ATTN: JLA, R. Haag

DEPARTMENT OF DEFENSE (Continued)

National Security Agency
ATTN: B-3, F. Leonard
ATTN: W-32, O. Bartlett
ATTN: R-52, J. Skillman

Undersecretary of Def. for Rsch. & Engrg.
ATTN: Strategic & Space Systems (OS)

WWMCCS System Engineering Org.
ATTN: R. Crawford

DEPARTMENT OF THE ARMY

Assistant Chief of Staff for Automation & Comm.
Department of the Army
ATTN: DAAC-ZT, P. Kenny

Atmospheric Sciences Laboratory
U.S. Army Electronics R&D Command
ATTN: DELAS-EO, F. Niles

BMD Advanced Technology Center
Department of the Army
ATTN: ATC-O, W. Davies
ATTN: ATC-T, M. Capps
ATTN: ATC-R, D. Russ

BMD Systems Command
Department of the Army
2 cy ATTN: BMDSC-HW

Deputy Chief of Staff for Ops. & Plans
Department of the Army
ATTN: DAMO-RQC

Electronics Tech. & Devices Lab.
U.S. Army Electronics R&D Command
ATTN: DELET-ER, H. Bomke

Harry Diamond Laboratories
Department of the Army
ATTN: DELHD-N-P, F. Wimenitz
ATTN: DELHD-I-TL, M. Weiner
ATTN: DELHD-N-P
ATTN: DELHD-N-RB, R. Williams

U.S. Army Comm.-Elec. Engrg. Instal. Agency
ATTN: CCC-CED-CCO, W. Neuendorf
ATTN: CCC-EMEO-PED, G. Lane
ATTN: CCC-EMEO, W. Nair

U.S. Army Communications Command
ATTN: CC-OPS-W
ATTN: CC-OPS-WR, H. Wilson

U.S. Army Communications R&D Command
ATTN: DRDCO-COM-RY, W. Kesselman

U.S. Army Foreign Science & Tech. Ctr.
ATTN: DRXST-SD

U.S. Army Materiel Dev. & Readiness Cmd.
ATTN: DRCLDC, J. Bender

DEPARTMENT OF THE ARMY (Continued)

U.S. Army Missile Intelligence Agency
ATTN: J. Gamble

U.S. Army Nuclear & Chemical Agency
ATTN: Library

U.S. Army Satellite Comm. Agency
ATTN: Document Control

U.S. Army TRADOC Systems Analysis Activity
ATTN: ATAA-TDC
ATTN: ATAA-PL
ATTN: ATAA-TCC, F. Payan, Jr.

DEPARTMENT OF THE NAVY

Joint Cruise Missiles Project
Department of the Navy
ATTN: JCMG-707

Naval Air Development Center
ATTN: Code 6091, M. Setz

Naval Air Systems Command
ATTN: PMA 271

Naval Electronic Systems Command
ATTN: PME 117-20
ATTN: PME 106-4, S. Kearney
ATTN: PME 117-211, B. Kruger
ATTN: PME 106-13, T. Griffin
ATTN: PME 117-2013, G. Burnhart
ATTN: Code 3101, T. Hughes
ATTN: Code 501A

Naval Intelligence Support Ctr.
ATTN: NISC-50

Naval Ocean Systems Center
ATTN: Code 5322, M. Paulson
ATTN: Code 532, J. Bickel
3 cy ATTN: Code 5324, W. Moler

Naval Research Laboratory
ATTN: Code 4700, T. Coffey
ATTN: Code 7500, B. Wald
ATTN: Code 7550, J. Davis
ATTN: Code 4780, S. Ossakow

Naval Space Surveillance System
ATTN: J. Burton

Naval Surface Weapons Center
ATTN: Code F31

Naval Surface Weapons Center
ATTN: Code F-14, R. Butler

Naval Telecommunications Command
ATTN: Code 341

Office of Naval Research
ATTN: Code 465
ATTN: Code 421
ATTN: Code 420

Office of the Chief of Naval Operations
ATTN: OP 981N
ATTN: OP 65
ATTN: OP 941D

DEPARTMENT OF THE NAVY (Continued)

Strategic Systems Project Office
Department of the Navy
ATTN: NSP-2722, F. Wimberly
ATTN: NSP-43
ATTN: NSP-2141

DEPARTMENT OF THE AIR FORCE

Aerospace Defense Command
Department of the Air Force
ATTN: DC, T. Long

Air Force Geophysics Laboratory
ATTN: OPR-1, J. Ulwick
ATTN: PHP, J. Aarons
ATTN: LKB, K. Champion
ATTN: OPR, A. Stair
ATTN: OPR, H. Gardiner
ATTN: PHI, J. Buchau
ATTN: PHP, J. Mullen

Air Force Weapons Laboratory
Air Force Systems Command
ATTN: SUL
ATTN: DYC

Air Force Wright Aeronautical Laboratories
ATTN: AAD, W. Hunt
ATTN: A. Johnson

Air Logistics Command
Department of the Air Force
ATTN: OO-ALC/MM, R. Blackburn

Assistant Chief of Staff
Intelligence
Department of the Air Force
ATTN: INED

Assistant Chief of Staff
Studies & Analyses
Department of the Air Force
ATTN: AF/SASC, G. Zank
ATTN: AF/SASC, W. Adams

Ballistic Missile Office
Air Force Systems Command
ATTN: MNHH, M. Baran
ATTN: MNHL, S. Kennedy
ATTN: MNHH

Deputy Chief of Staff
Operations Plans and Readiness
Department of the Air Force
ATTN: AFXOKCD
ATTN: AFXOKT
ATTN: AFXOKS
ATTN: AFXOXFD

Deputy Chief of Staff
Research, Development, & Acq.
Department of the Air Force
ATTN: AFRDSP
ATTN: AFRDSS
ATTN: AFRDS
ATTN: AFRDQ

Electronic Systems Division
Department of the Air Force
ATTN: DCKC, J. Clark

DEPARTMENT OF THE AIR FORCE (Continued)

Electronic Systems Division
Department of the Air Force
ATTN: XRW, J. Deas

Electronic Systems Division
Department of the Air Force
ATTN: YSM, J. Kobelski
ATTN: YSEA

Foreign Technology Division
Air Force Systems Command
ATTN: TQTD, B. Ballard
ATTN: NIIS, Library
ATTN: SDEC, A. Oakes

Headquarters Space Division
Air Force Systems Command
ATTN: SKA, C. Rightmyer
ATTN: SKA, M. Clavin

Headquarters Space Division
Air Force Systems Command
ATTN: SZJ
ATTN: SZJ, W. Mercer
ATTN: SZJ, L. Doan

Rome Air Development Center
Air Force Systems Command
ATTN: OCS, V. Coyne
ATTN: TSLD

Rome Air Development Center
Air Force Systems Command
ATTN: EEP

Strategic Air Command
Department of the Air Force
ATTN: OOKSN
ATTN: DCX
ATTN: XPFS
ATTN: DCXF
ATTN: NRT
ATTN: DCXT
ATTN: DCXT, T. Jorgensen

DEPARTMENT OF ENERGY CONTRACTORS

EG&G, Inc.
Los Alamos Division
ATTN: J. Colvin
ATTN: D. Wright

Lawrence Livermore National Laboratory
ATTN: L-31, R. Hager
ATTN: Technical Information Dept. Library
ATTN: L-389, R. Ott

Los Alamos National Scientific Laboratory
ATTN: MS 664, J. Zinn
ATTN: R. Taschek
ATTN: D. Simons
ATTN: P. Keaton
ATTN: E. Jones
ATTN: D. Westervelt

Sandia National Laboratories
Livermore Laboratory
ATTN: B. Murphrey
ATTN: T. Cook

DEPARTMENT OF ENERGY CONTRACTORS (Continued)

Sandia National Laboratories
ATTN: Space Project Div.
ATTN: ORG 1250, W. Brown
ATTN: 3141
ATTN: D. Dahlgren
ATTN: D. Thornbrough
ATTN: ORG 4241, T. Wright

OTHER GOVERNMENT AGENCIES

Central Intelligence Agency
ATTN: OSI/PSTD

Department of Commerce
National Bureau of Standards
ATTN: R. Moore

Department of Commerce
National Oceanic & Atmospheric Admin.
ATTN: R. Grubb

Institute for Telecommunications Sciences
ATTN: L. Berry
ATTN: D. Crombie
ATTN: W. Utlauf
ATTN: A. Jean

U.S. Coast Guard
ATTN: G-DOE-3/TP54, B. Romine

DEPARTMENT OF DEFENSE CONTRACTORS

Aerospace Corp.
ATTN: S. Bower
ATTN: N. Stockwell
ATTN: F. Morse
ATTN: T. Salmi
ATTN: I. Garfunkel
ATTN: D. Olsen
ATTN: V. Josephson
ATTN: R. Slaughter

University of Alaska
ATTN: N. Brown
ATTN: T. Davis
ATTN: Technical Library

Analytical Systems Engineering Corp.
ATTN: Radio Sciences

Analytical Systems Engineering Corp.
ATTN: Security

Barry Research Corporation
ATTN: J. McLaughlin

BDM Corp.
ATTN: T. Neighbors
ATTN: L. Jacobs

Berkeley Research Associates, Inc.
ATTN: J. Workman

Boeing Co.
ATTN: G. Hall
ATTN: S. Tashird
ATTN: M-S 42-33, J. Kennedy

DEPARTMENT OF DEFENSE CONTRACTORS (Continued)

University of California at San Diego
ATTN: H. Booker

Charles Stark Draper Lab., Inc.
ATTN: D. Cox
ATTN: J. Gilmore

Computer Sciences Corp.
ATTN: H. Blank

Comsat Labs.
ATTN: R. Taur
ATTN: G. Hyde

Cornell University
ATTN: D. Farley, Jr.

Electrospace Systems, Inc.
ATTN: H. Logston

ESL, Inc.
ATTN: J. Marshall

Ford Aerospace & Communications Corp.
ATTN: J. Mattingley

General Electric Co.
ATTN: A. Harcar
ATTN: M. Bortner

General Electric Co.
ATTN: A. Steinmayer
ATTN: C. Zierdt

General Electric Co.
ATTN: F. Reibert

General Electric Company—TEMPO
ATTN: W. Knapp
ATTN: T. Stevens
ATTN: W. McNamara
ATTN: M. Stanton
ATTN: D. Chandler
ATTN: DASIAC

General Electric Tech. Services Co., Inc.
ATTN: G. Millman

General Research Corp.
ATTN: J. Garbarino
ATTN: J. Ise, Jr.

GTE Sylvania, Inc.
ATTN: M. Cross

HSS, Inc.
ATTN: D. Hansen

IBM Corp.
ATTN: F. Ricci

University of Illinois
ATTN: K. Yeh

Institute for Defense Analyses
ATTN: E. Bauer
ATTN: J. Bengston
ATTN: J. Aein
ATTN: H. Wolfhard

DEPARTMENT OF DEFENSE CONTRACTORS (Continued)

International Tel. & Telegraph Corp.
ATTN: G. Wetmore
ATTN: Technical Library

JAYCOR
ATTN: S. Goldman

JAYCOR
ATTN: D. Carlos

Johns Hopkins University
ATTN: T. Potemra
ATTN: P. Komiske
ATTN: Document Librarian
ATTN: T. Evans
ATTN: J. Newland
ATTN: B. Wise

Kaman Sciences Corp.
ATTN: J. Meagher

Loral Space & Communications
ATTN: J. Jacobs

Lockheed Corp.
ATTN: J. L. Smith

McDonnell Douglas Corp., Inc.
ATTN: V. A. Smith

McDonnell Douglas Corp., Inc.
ATTN: W. J. Mullin
ATTN: J. C. Miller

McDonnell Douglas Corp., Inc.
ATTN: J. C. Miller

McDonnell Douglas Corp., Inc.
ATTN: J. C. Miller

McDonnell Douglas Corp., Inc.
ATTN: R. Heffner

McDonnell Douglas Corp.
ATTN: N. Harris
ATTN: R. Halprin
ATTN: J. Moule
ATTN: G. Mroz
ATTN: W. Olson

Meteor Communications Consultants
ATTN: R. Leader

Mission Research Corp.
ATTN: S. Gutsche
ATTN: F. Fajen
ATTN: R. Kilb
ATTN: D. Sowle
ATTN: D. Sappenfield
ATTN: R. Bogusch
ATTN: R. Hendrick

Mitre Corp.
ATTN: C. Callahan
ATTN: G. Harding
ATTN: A. Kymmel
ATTN: B. Adams

DEPARTMENT OF DEFENSE CONTRACTORS (Continued)

Mitre Corp.
ATTN: M. Horrocks
ATTN: W. Hall
ATTN: W. Foster
ATTN: J. Wheeler

Pacific-Sierra Research Corp.
ATTN: E. Field, Jr.

Pennsylvania State University
ATTN: Ionospheric Research Lab.

Photometrics, Inc.
ATTN: I. Kofsky

Physical Dynamics, Inc.
ATTN: E. Fremouw

R & D Associates
ATTN: B. Gabbard
ATTN: C. Greifinger
ATTN: W. Wright, Jr.
ATTN: R. Lelevier
ATTN: R. Turco
ATTN: H. Ory
ATTN: M. Gantsweg
ATTN: C. MacDonald
ATTN: F. Gilmore
ATTN: W. Karzas
ATTN: P. Haas

R & D Associates
ATTN: B. Yoon
ATTN: L. Delaney

Rand Corp.
ATTN: C. Crain
ATTN: E. Bedrozian

Riverside Research Institute
ATTN: V. Trapani

Rockwell International Corp.
ATTN: J. Kristof

Science Applications, Inc.
ATTN: J. McDougall
ATTN: D. Hamlin
ATTN: C. Smith
ATTN: D. Sachs
ATTN: L. Linson
ATTN: E. Straker

DEPARTMENT OF DEFENSE CONTRACTORS (Continued)

Santa Fe Corp.
ATTN: E. Ortlib

Science Applications, Inc.
ATTN: D. Divis

Science Applications, Inc.
ATTN: SZ

Science Applications, Inc.
ATTN: J. Cockayne

SRI International
ATTN: R. Leadabrand
ATTN: M. Baron
ATTN: R. Livingston
ATTN: W. Chesnut
ATTN: G. Price
ATTN: W. Jaye
ATTN: D. Neilson
ATTN: A. Burns
ATTN: C. Rino
ATTN: G. Smith
10 cy ATTN: R. Tsunoda

Technology International Corp.
ATTN: W. Boquist

Teledyne Brown Engineering
ATTN: R. Deliberis

Tri-Com, Inc.
ATTN: D. Murray

TRW Defense & Space Sys. Group
ATTN: S. Altschuler
ATTN: D. Dee
ATTN: R. Plebuch

Utah State University
ATTN: L. Jensen
ATTN: K. Baker

Visidyne, Inc.
ATTN: C. Humphrey
ATTN: J. Carpenter